ARTICLES
https://doi.org/10.1038/s41551-022-00909-y

nature biomedical engineering

Mapping and targeted viral activation of pancreatic nerves in mice reveal their roles in the regulation of glucose metabolism

M. Jimenez-Gonzalez[1], R. Li[1], L. E. Pomeranz[2], A. Alvarsson[1], R. Marongiu[3], R. F. Hampton[1], M. G. Kaplitt[3], R. C. Vasavada[4], G. J. Schwartz[5] and S. A. Stanley[1,6] ✉

A lack of comprehensive mapping of ganglionic inputs into the pancreas and of technology for the modulation of the activity of specific pancreatic nerves has hindered the study of how they regulate metabolic processes. Here we show that the pancreas-innervating neurons in sympathetic, parasympathetic and sensory ganglia can be mapped in detail by using tissue clearing and retrograde tracing (the tracing of neural connections from the synapse to the cell body), and that genetic payloads can be delivered via intrapancreatic injection to target sites in efferent pancreatic nerves in live mice through optimized adeno-associated viruses and neural-tissue-specific promoters. We also show that, in male mice, the targeted activation of parasympathetic cholinergic intrapancreatic ganglia and neurons doubled plasma-insulin levels and improved glucose tolerance, and that tolerance was impaired by stimulating pancreas-projecting sympathetic neurons. The ability to map the peripheral ganglia innervating the pancreas and to deliver transgenes to specific pancreas-projecting neurons will facilitate the examination of ganglionic inputs and the study of the roles of pancreatic efferent innervation in glucose metabolism.

The pancreas is critical to normal metabolism and digestion, and neural signals play crucial roles in regulating these functions. However, the precise contributions of pancreatic nerves to metabolic control and digestive processes remain ill-defined because of the lack of sufficient understanding of ganglionic inputs into the pancreas and of tools with the specificity to modulate pancreatic nerve function in isolation. To understand the physiological roles of defined pancreatic nerves and how these are disrupted in pancreatic disease, approaches that enable the detailed mapping of pancreatic ganglia and the precise regulation of pancreatic nerve activity are needed. By applying tissue clearing with retrograde tracing and combinatorial approaches to target the delivery of adeno-associated viruses (AAVs) to pancreatic nerves, in this work we have mapped the ganglionic inputs to the pancreas and identified glucose-regulation roles of the pancreatic parasympathetic and sympathetic nerves.

The pancreas is a complex organ with both exocrine and endocrine components. The exocrine pancreas, comprising 95% of pancreatic mass, produces enzymes such as trypsin and bicarbonate for digestion[1]. The endocrine pancreas consists of scattered cell clusters, the Islets of Langerhans. The major endocrine cell types, β-cells (insulin production), α-cells (glucagon production), δ-cells (somatostatin production) and PP cells (for pancreatic polypeptide (PP) production) together act to maintain blood glucose in a narrow range[2]. These diverse pancreatic functions must react rapidly to ingested nutrients and require tight coordination with other organs. Ingested food triggers the release of exocrine secretions and pancreatic hormones, even before nutrients are absorbed. Exocrine secretions are synchronized with digestion, and pancreatic hormone release must be coordinated with other metabolically relevant organs, such as the liver, as well as with fat and muscle. Neural signals are critical to these processes[3–7].

The need for new methods to unravel the roles of pancreatic innervation is illustrated by the limitations of previous anatomical and functional studies. Neural signals are relayed between the central nervous system (CNS) and peripheral organs, such as the pancreas, by autonomic (sympathetic and parasympathetic) and non-vagal sensory and efferent nerves, which together make up the peripheral nervous system (PNS). Tissue clearing and three-dimensional (3D)-imaging techniques of whole organ/tissue structures have confirmed dense pancreatic innervation. Mouse and human pancreata, and particularly the pancreatic islets, are richly innervated by autonomic and sensory fibres[8–10]. Previous studies have examined the intrinsic and extrinsic ganglia providing inputs to specific pathways in pancreatic innervation. Dense sensory innervation[11] transmits information to the CNS via vagal and spinal nerves, with studies in mice showing cell bodies located in nodose ganglia (NG) and dorsal root ganglia (DRG), respectively[12,13]. Examination of sympathetic pre-ganglionic neurons in rats demonstrated that they emerge from the spinal cord and project via splanchnic nerves to post-ganglionic neurons in the coeliac ganglia (CG). Post-ganglionic sympathetic fibres directly innervate acinar cells, islets and vasculature, as well as intrapancreatic ganglia (IPG)[14]. Studies in guinea pigs showed that parasympathetic input to the pancreas travels via the vagus nerve to innervate a distributed network of intrinsic intrapancreatic ganglia. Post-ganglionic neurons from intrapancreatic ganglia then project to acinar cells, islets and vasculature[15–17]. In addition, enteric neurons in rats and guinea pigs project from the stomach and duodenum

[1]Diabetes, Obesity and Metabolism Institute, Icahn School of Medicine at Mount Sinai, New York, NY, USA. [2]Laboratory of Molecular Genetics, The Rockefeller University, New York, NY, USA. [3]Laboratory of Molecular Neurosurgery, Department of Neurological Surgery, Weill Cornell Medical College, New York, NY, USA. [4]Department of Translational Research and Cellular Therapeutics, City of Hope, Duarte, CA, USA. [5]Departments of Medicine and Neuroscience, Albert Einstein College of Medicine, Bronx, NY, USA. [6]Nash Family Department of Neuroscience and Friedman Brain Institute, Icahn School of Medicine at Mount Sinai, New York, NY, USA. ✉e-mail: sarah.stanley@mssm.edu

to the pancreas[18–20]. However, these anatomical studies cut across several species, examine defined pathways in isolation, and use multiple different retrograde tracing dyes/labelled proteins, hence our understanding of the relative contributions of these pathways to pancreatic neural regulation in a single species is incomplete. Here we use the tissue-clearing technique, immunolabelling-enabled 3D imaging of solvent-cleared organs (iDISCO+)[21], combined with neuronal tracing to visualize, map and characterize the intrinsic and extrinsic sympathetic, parasympathetic and sensory ganglia innervating the pancreas in mice.

Similarly, electrical stimulation and nerve transection studies have demonstrated the importance of neural inputs in pancreatic function but with conflicting results[22] and substantial gaps. Electrical stimulation of sympathetic splanchnic nerves largely leads to decreased insulin release, increased glucagon secretion[23,24] and vasoconstriction, resulting in increased blood glucose with little or no effect on exocrine function[25,26]. However, effects on insulin release have been conflicting[27,28]. In contrast, electrical stimulation of the parasympathetic vagus nerve has been reported to increase plasma insulin, glucagon and PP to decrease blood glucose overall;[29,30] reduce insulin to increase glucose;[22] or have no effect[31]. Similarly, the effects of vagotomy are variable. In some studies, vagotomy abolishes anticipatory insulin release and pancreatic exocrine secretion[32,33], while in others, insulin is unaffected but glucagon responses to glucose are abnormal[34]. It is known that pancreatic sensory nerves are critical to pain[35], but their contributions to metabolic regulation and digestion are less well understood. Sensory nerve ablation has been reported to either improve glucose-stimulated insulin secretion or have no effect[13,36], while the sensory neurotransmitter Substance P inhibited exocrine secretion[37]. Together, these studies provide valuable insights into the critical roles of neural signals in regulating pancreatic function. However, they modulate vagal, splanchnic or spinal nerves that project to multiple organs and modify activity in both sensory (afferent) and motor (efferent) pathways simultaneously. As a result, we do not know whether alterations in pancreatic function are indirect responses to modulating hepatic, adipose or other organ function, or which pancreatic nerves/pathways regulate specific functions. Targeted approaches to control pancreatic nerve activity are required to assess the precise neural pathways regulating pancreatic function and the exact roles of defined pancreatic nerves.

Virus-mediated delivery of neuromodulatory tools provides access to defined neural populations to assess their physiological roles, and adeno-associated viruses (AAVs) are ideal vectors for gene delivery. AAVs transduce cells with high efficiency and induce minimal immune response, resulting in prolonged gene expression[38]. However, AAV serotypes vary widely in tropism and infection efficiency;[39] while several serotypes have been used for retrograde spread from peripheral organs to the spinal cord and sensory ganglia[40], the best viral methods to target pancreatic innervation are unknown. Here we optimized AAV serotypes, promoters and delivery routes to specifically target pancreatic efferent and afferent nerves. This approach allows delivery of genetically encoded tools, such as chemogenetics, to provide long-lasting, temporally-regulated neuronal modulation of transduced neurons across an entire organ in freely moving animals[41], making it well-suited for dissecting the roles of specific pancreatic nerves.

Here we present a detailed map of the sympathetic, parasympathetic and spinal sensory inputs into pancreatic innervation using iDISCO+ in mice. We identified AAV serotypes, promoters and delivery routes to specifically target pancreatic nerves. We found that AAV8 preferentially transduces efferent pathways (CG neurons and intrapancreatic ganglia), whereas rAAV2-retro largely targets afferent neurons in the NG. Combining precise anatomical delivery with appropriate viral titres, neuronal promoters and microRNA target sites, we accurately targeted gene delivery to pancreatic nerves without expression in exocrine or endocrine pancreatic tissue or off-target organs. To interrogate the physiological roles of pancreatic efferent nerves, we used our optimized viral targeting strategy to deliver chemogenetic constructs for cell-type-specific neural modulation. Using this approach, we demonstrated that activation of pancreatic efferent parasympathetic neurons in intrinsic intrapancreatic ganglia substantially increased plasma insulin and improved glucose metabolism in vivo in male, but not in female mice, whereas the activation of pancreatic efferent sympathetic neurons in extrinsic coeliac ganglia impaired glucose metabolism.

Results

The pancreas is innervated by multiple peripheral ganglia. Peripheral ganglia can regulate organ function, integrate inputs and may act independently from central control, hence delineating the ganglia contributing to pancreatic innervation provides important information about its neural regulation. The pancreas is highly innervated by the sympathetic, parasympathetic and sensory PNS (Fig. 1a). Dense networks of nerve fibres across the exocrine and endocrine pancreas were confirmed by whole pancreas tissue-clearing and staining for pathway-specific neural markers: vesicular acetylcholine transporter (VAChT) for efferent parasympathetic innervation and tyrosine hydroxylase (TH) for efferent sympathetic innervation (Fig. 1b, and Supplementary Videos 1 and 2). To determine the relative contribution of the autonomic and sensory inputs to pancreatic innervation, we performed intrapancreatic injections of the non-viral tracer, cholera toxin β (CTβ) and quantified CTβ+ pancreas-projecting neurons in cleared extrinsic and intrinsic ganglia: CG, NG, DRG comprising the extrinsic ganglia, and intrapancreatic ganglia comprising intrinsic ganglia. Tissue clearing and confocal imaging allowed quantification of neurons (labelled and unlabelled) and 3D distribution in these ganglia (Fig. 1c). NG and DRG are composed of a similar number of neurons (1,000.5 ± 319.9 and 1,042.8 ± 217.3 neurons, respectively), while CG had almost 50% more neurons (1,470.9 ± 556.7 neurons) (Supplementary Table 1). CTβ+ cell bodies were found in vagal sensory neurons in the NG (7.47 ± 8.58% NG neurons) and spinal sensory neurons in DRG (5.30 ± 3.6% DRG neurons). Vagal and spinal sensory neurons were equally labelled by CTβ, with no substantial difference in the number of CTβ+ neurons between left and right NG or DRG. Pancreas-projecting neurons were present in the sympathetic motor neurons of the CG (6.08 ± 2.12% CG neurons) (Fig. 1c,d). Sympathetic CG neurons form a substantial proportion of motor inputs into the pancreas (19 ± 13.58% of CTβ+ neurons) (Extended Data Fig. 1a). However, we detected very few intrapancreatic ganglia with CTβ+ cells (Fig. 1c). In contrast to other ganglia such as the stellate ganglia, CTβ+ neurons were distributed throughout CG, NG and individual DRG without evidence of a viscerotopic map (Supplementary Video 3).

Chemically and functionally discrete neural populations exist in peripheral ganglia and neurons expressing distinct markers often have different sizes[42]. To examine heterogeneity among pancreas-projecting CTβ+ neurons, we assessed the size distribution of CTβ+ cells in peripheral ganglia (Fig. 1e). In the CG, the majority of labelled neurons were less than 10,000 μm^3 (equivalent to a diameter of 26 μm, assuming a sphere), but sparse populations of large neurons up to 30,000 μm^3 were also present. CTβ+ cell bodies in DRG had a similar size distribution to those in CG, including larger neurons, while most pancreas-projecting neurons in NG were less than 5,000 μm^3 (equivalent to a diameter of 20 μm). Although there was no substantial difference in the number of labelled neurons in left and right NG or DRG after CTβ injection into the pancreas (Fig. 1e), there were substantial differences in the size distribution of CTβ-labelled neurons. Labelled neurons in the right NG were substantially larger than those in the left NG, while neurons in the right DRG were substantially smaller than

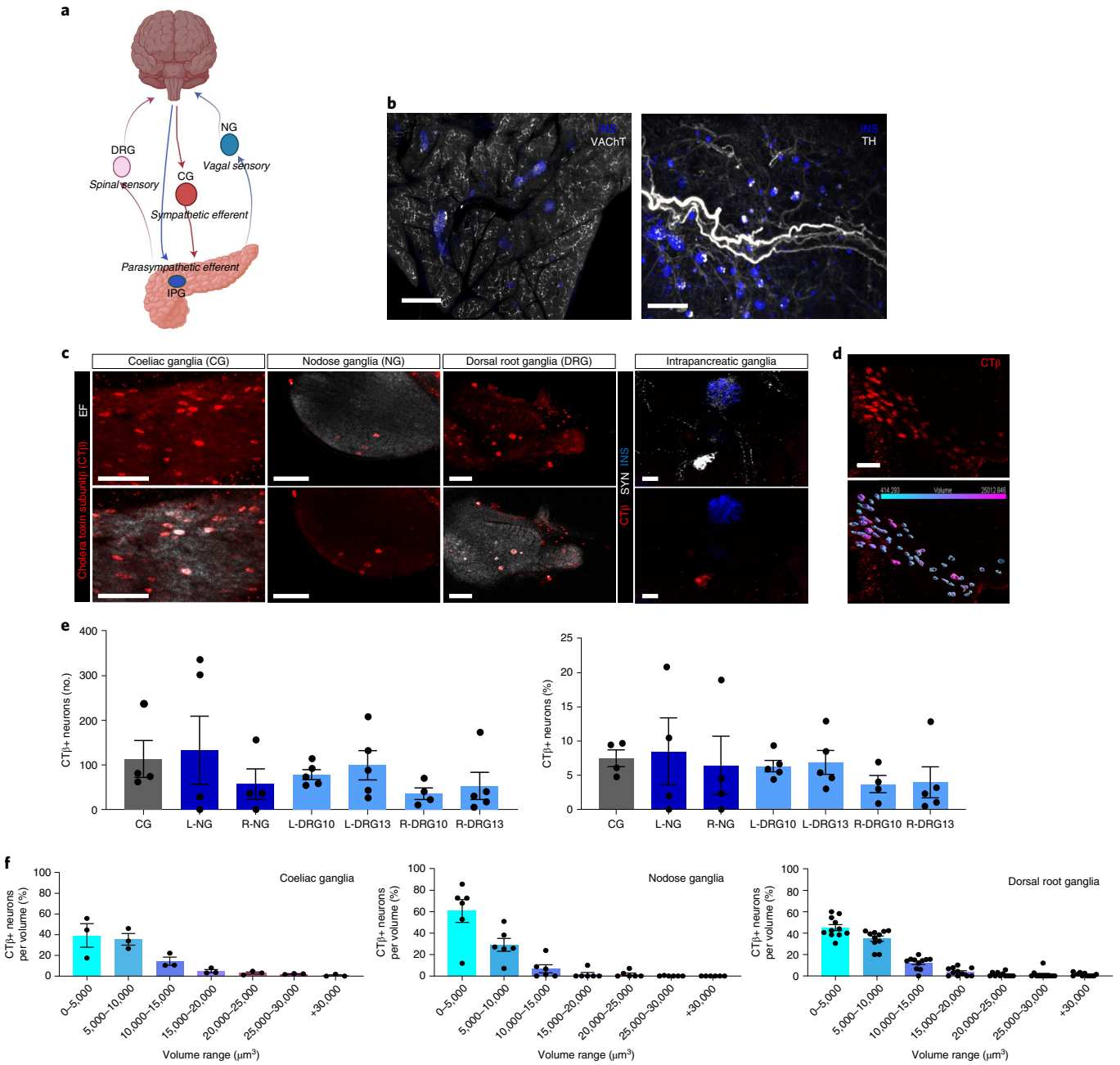

Fig. 1 | The pancreas is innervated by neurons in coeliac, nodose, dorsal root and intrapancreatic ganglia. a, Schematic representation of pancreas innervation. **b**, Maximum projections of lightsheet microscopy images of mouse pancreatic samples cleared with iDISCO+ and stained for insulin (blue) and vesicular acetylcholine transporter, VAChT (white, left), or tyrosine hydroxylase, TH (white, right). Scale bars, 300 μm. **c**, Representative confocal images of CTβ+ pancreas-innervating neurons (red, top row) in cleared peripheral ganglia (CG, NG, DRG and IPG) after intrapancreatic injection. Bottom row shows CTβ+ pancreas-innervating neurons (red) and endogenous fluorescence (EF) (white) for CG, NG and DRG. Upper right panel shows synapsin (SYN) marking intrapancreatic ganglia (white) and insulin (blue), bottom right panel shows CTβ+ pancreas-innervating neurons (red) and insulin (blue). Scale bars, 100 μm. **d**, Representative segmentation of CTβ+ pancreas-innervating neurons in CG showing CTβ+ pancreas-innervating neurons (red, top left side) and 3D volumes colour-coded for size (bottom left side). Two independent studies (3 and 2 ganglia, respectively). Scale bar, 100 μm. **e**, Quantification of CTβ+ pancreas-innervating neurons as total number per ganglion (left) and percentage of the total neurons per ganglion (number of CTβ+ pancreas-innervating neurons in specified ganglia/total number of neurons in specified ganglia) (right) after intrapancreatic injection of CTβ. Data are shown for left and right DRG at T10 and T13 (L-DRG10, L-DRG13, R-DRG10 and R-DRG13). Biologically independent sample numbers: CG, 4 samples; L-NG, 4 samples; R-NG, 4 samples; L-DRG10, 5 samples; L-DRG13, 5 samples; R-DRG10, 4 samples; and R-DRG13, 5 samples. **f**, Volume distribution of CTβ+ pancreas-innervating neurons within each ganglion in CG (left), NG (middle) and DRG (right) ($N=3$ mice). All data are represented as mean ± SEM. Individual data points represent individual ganglia. Statistical analyses are described in Supplementary Table 2. Figure 1a was created with BioRender.com.

those in the left DRG (Extended Data Fig. 1b). These results suggest differences in the neurochemical identity of CTβ+ labelled neurons in the left and right NG and DRG.

Together these data demonstrate the feasibility of tissue clearing for 3D visualization of retrograde-labelled extrinsic and intrinsic pancreatic ganglia to allow quantification and characterization of

pancreas-projecting neurons. This approach revealed substantial efferent inputs to the pancreas from the CG in mice, confirmed substantial sensory innervation from both vagal and spinal sensory neurons and provided evidence that distinct neural populations in the left and right sensory ganglia innervate the pancreas.

AAVs selectively target pancreatic autonomic nerves. Neural tracing using dyes and non-viral tracers such as CTβ may have partial anterograde spread and high fluorescence at delivery sites, making visualization of short-range connections, such as those to intrapancreatic ganglia, difficult. In contrast, viral tracers can provide specific retrograde tracing and bright, long-term labelling by expressing fluorescent proteins[43]. Therefore, we decided to optimize retrograde viral tracing with AAV to better map the intrinsic and extrinsic ganglia innervating the pancreas. We performed intrapancreatic injection of AAV serotypes 6, 8, 9 and rAAV2-retro (AAVrg) to deliver the mCherry fluorescent reporter under the neuronal specific human Synapsin 1 promoter (AAV-hSyn-mCherry, 1×10^{11} viral genomes (vg) per mouse). There were substantially more mCherry+ neurons in cleared CG from mice injected with AAV8 and AAV9; these serotypes transduced similar proportions of neurons to the retrograde tracer CTβ. In contrast, CG from mice injected with AAV6 and AAVrg expressing hSyn-mCherry showed sparse labelling (Fig. 2a,c). In mice injected with AAV8-hSyn-mCherry, expression in CG was substantially higher than expression in NG or DRG, while AAV9-hSyn-mCherry expression in CG was substantially greater than expression in DRG. In contrast to AAV8 and 9, AAVrg preferentially labelled NG neurons (1.9 ± 0.9% neurons) (Fig. 2a,c), with 6-fold fewer neurons transduced in CG (0.35 ± 0.1% neurons) and minimal transduction in DRG (0.01 ± 0.01% neurons). However, AAVrg at this titre labelled NG neurons less robustly than CTβ. AAV6-hSyn-mCherry transduced CG, NG and DRG at low levels. Retrograde tracing with all serotypes labelled neurons in intrinsic IPG (Fig. 2b,d,e) and in the enteric nervous system (Extended Data Fig. 2a–c). These results demonstrate that AAV8 and 9 preferentially transduce efferent neurons innervating the pancreas. In contrast to the findings with CTβ, these studies indicate that both extrinsic CG and intrinsic IPG provide substantial autonomic efferent inputs into pancreatic tissue.

Previous reports suggest that gene expression in peripheral nerves after AAV delivery may decline rapidly using certain serotypes[44]. However, we found stable mCherry expression in CG up to 12 weeks after AAV8 delivery (Extended Data Fig. 2g), and expression in NG up to 4 weeks after AAV delivery (Fig. 2a,c). In addition, there was no evidence of apoptosis in peripheral ganglia after AAV delivery of fluorescent proteins, as reported for viral vectors such as pseudorabies virus (PRV) or adenovirus[45,46]. Cleaved caspase-3 immunostaining was absent in NG after intrapancreatic injection of AAVrg-hSyn-EGFP (1×10^{11} vg per mouse) but was clearly present after intrapancreatic injection of PRV-EGFP (2×10^{6} vg per mouse) as a positive control (Supplementary Fig. 1).

These results demonstrate that the choice of AAV serotype dramatically influences viral tropism when targeting pancreatic innervation. AAV8 and 9 selectively infect pancreatic autonomic efferent pathways to provide stable expression in intrinsic and extrinsic ganglia as well as peripheral neurons, while AAVrg shows some selectivity for vagal sensory neurons but lower transduction efficiency. The choice of AAV serotype can be exploited to selectively deliver genes to defined pancreatic innervation in mice.

Optimization of gene delivery into pancreatic innervation. To improve the efficiency of gene delivery to nerves innervating the pancreas, we compared transgene expression after intrapancreatic or intraductal AAV delivery. Intraductal infusion of cell dyes or viral vectors for islet infection is efficient, and controlled infusion using specific volumes and infusion rates can determine the extent of delivery into the pancreas[47]. For our studies, we chose to perform intraductal infusions at a volume of 150 µl and a rate of 6 µl min^{-1} to ensure a homogeneous distribution throughout the whole pancreas. We found a substantial increase in CTβ+ peripheral pancreatic neurons in CG with intraductal infusion ($P=0.057$) (Fig. 3a,b). There was no statistical difference in NG or DRG labelling (Fig. 3b).

Intraductal infusion allows delivery of larger volumes, so we assessed infection efficiency using increasing titres of AAV8-hSyn-mCherry. Specifically, we applied 5×1011 vg per mouse (5X original titre) and 1×1012 vg per mouse (10X original titre) via infusion, as well as 5×1011 vg per mouse (5X original titre) via intrapancreatic injection. Intraductal delivery of AAV8-hSyn-mCherry at the highest titre (10X) substantially increased mCherry expression in CG (Fig. 3c,d). MCherry+ cells in DRG and NG remained less than 1% even with increasing viral titres and/or intraductal infusion (Fig. 3e,f). Increasing viral titre also increased mCherry expression in intrapancreatic ganglia. We found that 26.8 ± 21.8% of intrapancreatic ganglia volume was mCherry+ after intraductal delivery of AAV8-hSyn-mCherry at 5×10^{11} vg per mouse. These results show that intraductal infusion and increasing viral titres improved transgene delivery to pancreas-projecting efferent neurons in coeliac and intrapancreatic ganglia with AAV.

Combined strategy for gene expression in pancreatic nerves. AAV8 effectively delivered fluorescent proteins for retrograde labelling of neural inputs to the pancreas. However, to use AAV for targeted modulation, we needed to assess off-target expression. We found no expression in heart, muscle or kidney (Extended Data Fig. 2a). AAV8, 9, 6 and retro hSyn-mCherry resulted in minimal expression in duodenum, mesentery, spleen and CNS (Extended Data Fig. 2b–d,f). However, despite using the neuronal promoter hSyn to drive gene expression, mCherry+ cells were present in hepatocytes for AAV9 and AAV8-hSyn-mCherry (Extended Data Fig. 2e).

We evaluated two methods to limit gene expression to pancreatic efferent neurons and maximize expression with AAV8. First, we assessed whether an alternative neuronal promoter, neuron-specific enolase (NSE)[48], might provide greater neuronal specificity after intrapancreatic delivery with AAV8. We compared transfection efficiency of plasmids expressing mCherry driven by the neuronal promoters hSyn or NSE[49], or a strong, ubiquitous synthetic mammalian promoter, JeT[50], in the human embryonic kidney HEK293T (HEK293T) and the murine neuroblastoma Neuro2a (N2A) cell lines (Supplementary Fig. 4a,b). MCherry expression was substantially greater with pNSE-mCherry than with phSyn-mCherry in N2A cells ($P=0.009$) (Extended Data Fig. 3c,d). Expression of pNSE-mCherry was also greater than phSyn-mCherry in transfected primary neurons from murine DRGs (Extended Data Fig. 3e). In vivo, AAV8-mCherry under hSyn or NSE promoters (1×10^{11} vg per mouse, intrapancreatic) effectively transduced CG neurons by retrograde spread (Extended Data Fig. 3f), but hepatocyte expression was evident with both (Extended Data Fig. 4g). These results show that NSE is a more robust neuronal promoter in vitro but not in vivo and did not restrict gene expression. Therefore, promoter specificity alone may be insufficient to limit transgene expression to pancreatic innervation.

To overcome off-target hepatocyte expression, we designed a liver-detargeting construct containing target sites (TS) for the binding of miR122, a microRNA highly expressed in the liver but not in neural tissue[51]. When miR122 binds to its target site, it recruits an RNA-induced silencing complex (RISC) and together these suppress the expression of the targeted gene[52] (Fig. 4a). We transfected plasmids containing mCherry under the hSyn promoter with or without the addition of miR122 TS (pAAV-hSyn-mCherry-miR122TS) into HEK293T cells and the alpha mouse liver 12 (AML12) cell line. We observed a substantial decrease in mCherry intensity in both cell

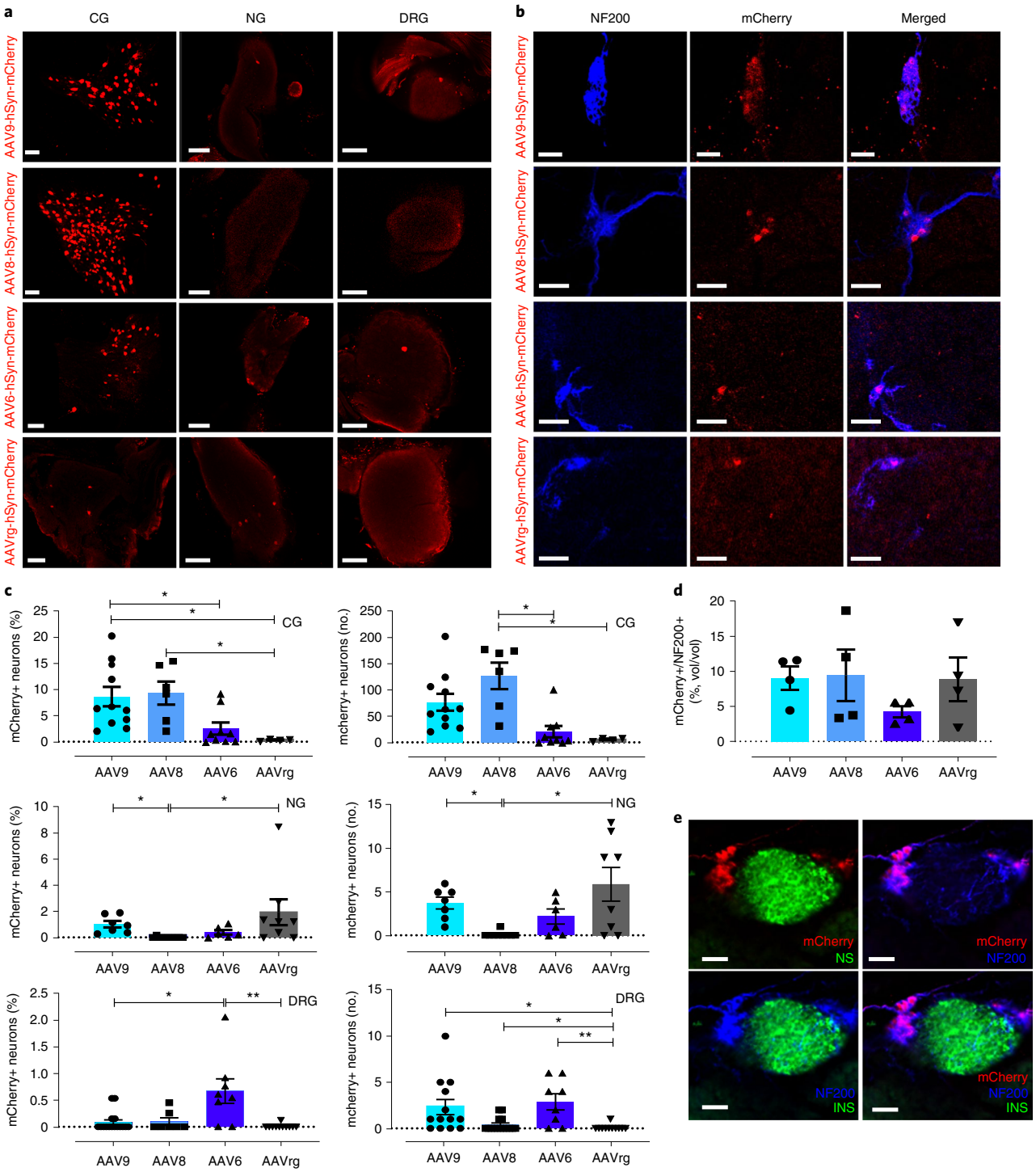

Fig. 2 | AAV serotypes selectively target pancreatic autonomic efferent and afferent nerves. a, Confocal images of iDISCO+ cleared CG, NG and DRG demonstrating mCherry+ pancreas-innervating neurons 4 weeks after intrapancreatic injection of AAV-hSyn-mCherry (top to bottom: serotypes 9, 8, 6 and rAAV2-retro (AAVrg)). Scale bars, 100 μm. $N = 4$ biologically independent samples. **b**, Confocal images of iDISCO+ cleared pancreas demonstrating mCherry+ neurons within intrapancreatic ganglia stained for NF200, 4 weeks after intrapancreatic injection of AAV-hSyn-mCherry. $N = 4$ biologically independent samples. Scale bars, 50 μm. **c**, Quantification of mCherry+ pancreas-innervating neurons in CG (top), NG (middle) and DRG (bottom), 4 weeks after intrapancreatic injection of AAV-hSyn-mCherry (left: percentage of total neurons per ganglion; right: total number per ganglion). **d**, Quantification of mCherry+ pancreas-innervating neurons in intrapancreatic ganglia, 4 weeks after intrapancreatic injection of AAV-hSyn-mCherry (mCherry volume as percentage of NF200+ volume of the ganglia). All data represented as mean ± SEM. **e**, Confocal image demonstrating specific neural expression of AAV8-hSyn-mCherry in intrapancreatic ganglia immunolabelled with NF200 with adjacent islet of Langerhans. Top left, mCherry (red) and insulin (green); top right, mCherry (red) and NF200 (blue); bottom left, NF200 (blue) and insulin (green); bottom right, mCherry (red), NF200 (blue) and insulin (green). Scale bars, 50 μm. Biologically independent samples: **c**, left and right: for CG $n = 11$ (AAV9), 6 (AAV8), 9 (AAV6), 4 (AAVrg); for NG $n = 7$ (AAV9), 9 (AAV8), 6 (AAV6), 8 (AAVrg); and for DRG: $n = 16$ (AAV9), 7 (AAV8), 8 (AAV6), 11 (AAVrg); **d**, $n = 4$ animals per group. Statistical analyses are described in Supplementary Table 2.

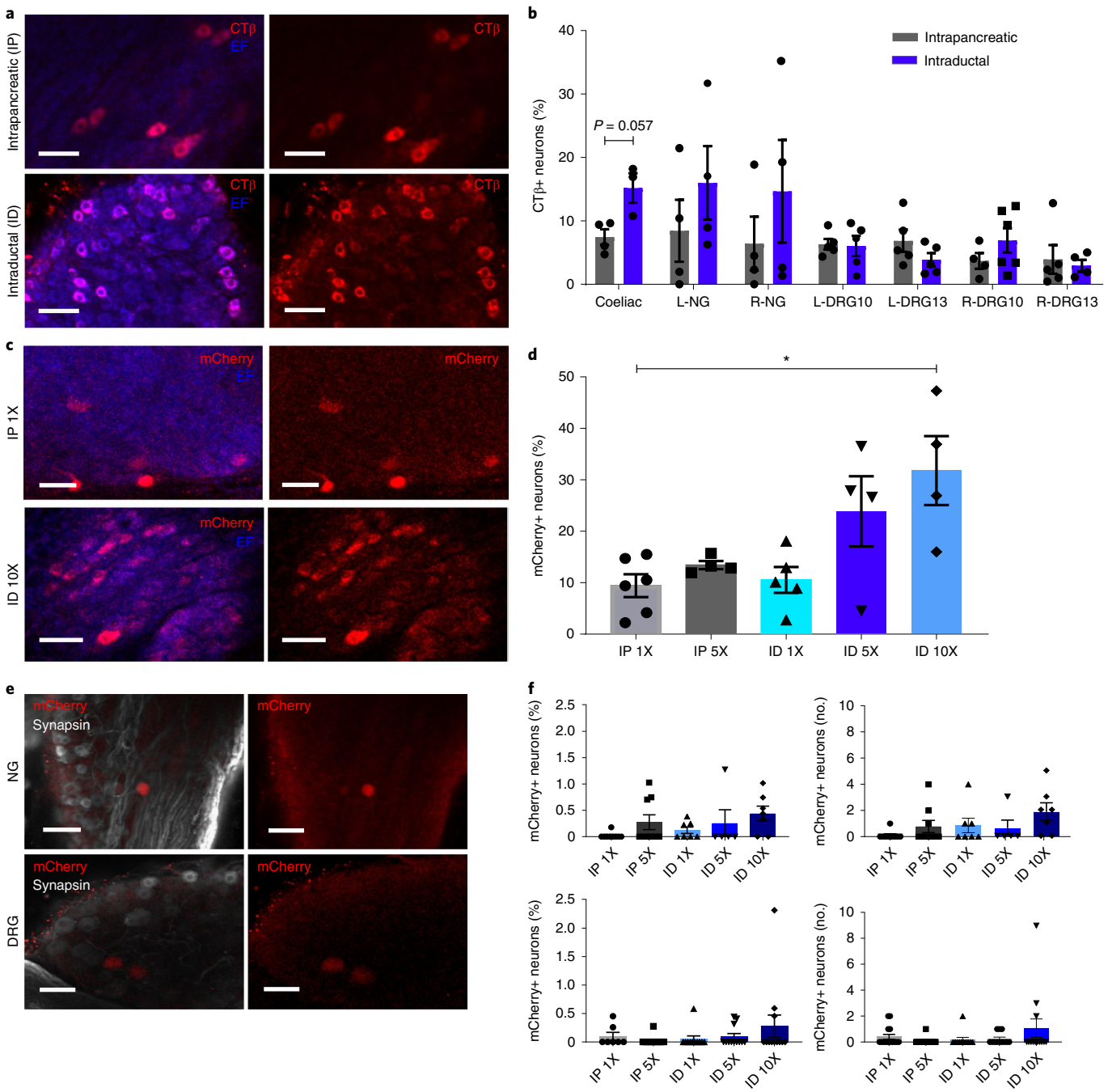

Fig. 3 | Optimization of gene delivery. a, Images of CTβ+ neurons in iDISCO+ cleared CG after CTβ delivery by IP injection (top) or ID infusion (bottom). Scale bars, 50 µm. Left, CTβ+ neurons (red) and endogenous fluorescence (EF, blue); right, CTβ+ neurons (red) alone. **b**, Quantification of CTβ neurons in peripheral ganglia after IP or ID delivery (percentage of total neurons). **c**, Images of mCherry+ neurons in iDISCO+ cleared CG after AAV8-hSyn-mCherry delivery (top: IP, dose 1X, 1×10^{11} vg; bottom: ID, dose 10X, 1X 1×10^{12} vg). Scale bars, 50 µm. **d**, Quantification of mCherry+ pancreas-innervating neurons in CG after AAV8-hSyn-mCherry delivery (IP doses: 1X, 1×10^{11} vg; 5X, 5×10^{11} vg; ID doses: 1X, 1×10^{11} vg; 5X, 5×10^{11} vg; 10X, 1X 1×10^{12} vg) (percentage of total neurons). **e**, Images of mCherry+ neurons in NG and DRG after AAV8-hSyn-mCherry delivery (ID dose 10X). Scale bars, 100 µm. **f**, Quantification of mCherry+ neurons in NG (top) and DRG (bottom) after AAV8-hSyn-mCherry delivery (IP doses: 1X, 1×10^{11} vg; 5X, 5×10^{11} vg; ID doses: 1X, 1×10^{11} vg; 5X, 5×10^{11} vg; 10X, 1X 1×10^{12} vg) (left: percentage of total neurons; right: total number per ganglion). All data represented as mean ± SEM. Biologically independent samples: for **b**, intrapancreatic: $N=4$ samples each for CG, L-NG, R-NG, L-DRG13 and R-DRG-10, and 5 samples each for L-DRG10 and R-DRG13. Intraductal: $N=3$ samples for CG, 4 samples each for L-NG, R-DRG10 and R-NG, 5 samples each for L-DRG10 and L-DRG13, and 6 samples for R-DRG13. For **d**: $N=6$ samples for IP1X, 4 each for IP5X, ID5X and ID10X, and 5 for ID1X. For **f**, top: $N=9$ samples each for IP1X and IP5X, 7 each for ID1X and ID10X, and 5 for ID5X. Bottom: $N=7$ samples for IP1X, 12 each for IP5X and ID10X, and 11 for ID1X. Statistical analyses are described in Supplementary Table 2.

lines using the liver-detargeting construct (Fig. 4b,c). The relative decrease in expression using the liver-detargeting construct was 30% for AML cells, in comparison with 15% for HEK293T cells. Next, we assessed in vivo mCherry expression in liver and CG after intrapancreatic delivery of AAV8-hSyn-mCherry-miR122TS or AAV8-hSyn-mCherry (1×10^{11} vg per mouse). Liver sections from

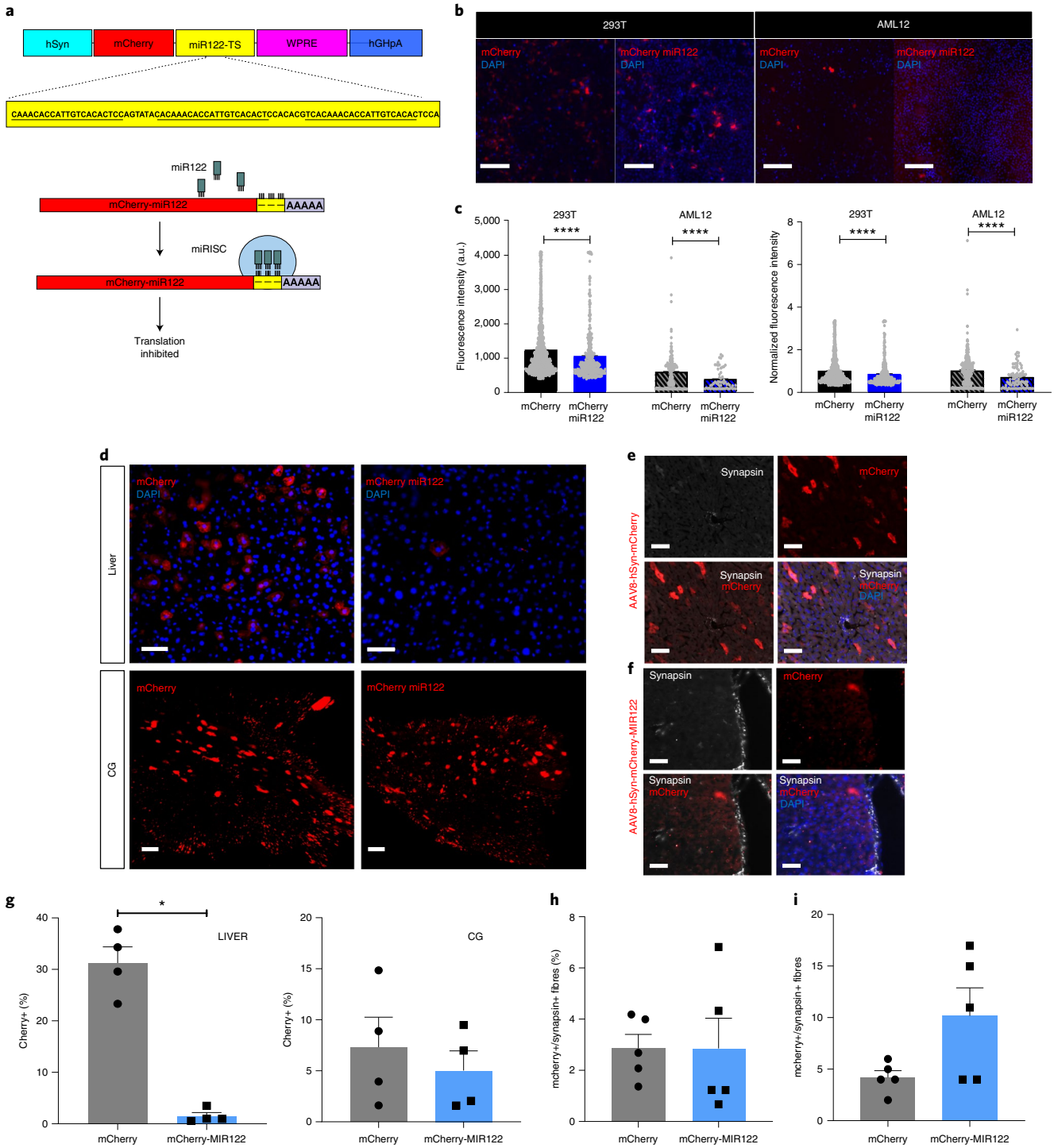

Fig. 4 | Combined strategy for restricted gene expression in pancreatic innervation. a, Schematic representation of liver-detargeting construct showing hSyn promoter, mCherry fluorescent protein, miR122 target site (miR122TS) in triplicate, woodchuck hepatitis virus post-transcriptional regulatory element (WPRE) and human growth hormone polyA (hGHpA). **b**, Representative immunofluorescence images of HEK293T (293T) and AML12 clonal cells after transfection with phSyn-mCherry and phSyn-mCherry-miR122TS (red). DAPI in blue. Scale bars, 200 µm. **c**, Quantification of absolute (left) and relative (right) fluorescence intensity of mCherry+ cells in transfected 293T and AML12 clonal cells. **d**, Representative immunofluorescence images of liver sections (top) and maximum projection of confocal images of mCherry+ pancreas-innervating neurons in CG (bottom), 4 weeks after intrapancreatic injection of AAV8-hSyn-mCherry (left) or AAV8-hSyn-mCherry-miR122TS (right). Scale bars, 25 µm for liver sections; 100 µm for CG. **e**, Representative immunofluorescence images of liver sections 4 weeks after intrapancreatic injection of AAV8-hSyn-mCherry, stained for mCherry (red) and synapsin (white), showing no overlap of mCherry+ off-target expression with synapsin+ fibres. Scale bar, 50 µm. **f**, Representative immunofluorescence images of liver sections 4 weeks after intrapancreatic injection of AAV8-hSyn-mCherry-miR122TS, stained for mCherry (red) and synapsin (white), showing a decrease in mCherry expression and no overlap mCherry+ off-target expression with synapsin+ fibres. Scale bar, 50 µm. **g**, Quantification of the percentage of mCherry+ cells in liver sections (left) and CG (right). **h**, Quantification of % mCherry+ in synapsin+ fibres. **i**, Raw overlap quantification of mCherry+ and synapsin+ fibres. All data represented as mean ± SEM. Statistical analyses are described in Supplementary Table 2.

animals injected with AAV8-hSyn-mCherry-miR122TS showed a 20-fold decrease in mCherry expression in hepatocytes compared with those injected with AAV8-hSyn-mCherry (Fig. 4g,e). Importantly, both constructs provided robust mCherry expression in CG (Fig. 4g,e). Both AAV8-hSyn-mCherry-miR122TS and AAV8-hSyn-mCherry labelled a small proportion of synapsin+ fibres in the liver (Fig. 4f–i). To determine the specificity of mCherry expression, we used dual retrograde tracing with Alexa-tagged CTβ from the liver and AAV8 hSyn-mCherry in the pancreas and identified co-localization of fluorophores in 10% of liver-projecting neurons and 17% of pancreas-projecting neurons. These findings suggest that a subpopulation of coeliac neurons may project to both pancreas and liver (Supplementary Fig. 2). These results demonstrate that the combination of a neuronal promoter and miR122 TS reduced off-target hepatocyte gene expression but maintained expression in pancreatic efferent innervation.

Pancreas parasympathetic activation improves glucose control. Next, we applied the viral serotypes, promoters and titres identified above to achieve highly targeted modulation of pancreatic innervation. First, we assessed whether pancreatic parasympathetic efferent innervation was sufficient to regulate glucose homoeostasis. Pancreatic cholinergic efferent neurons have their cell bodies in the intrapancreatic ganglia and fibres densely innervate pancreatic tissue, including islets, in mice. Published studies have used vagal stimulation and cholinergic agonists to assess the roles of parasympathetic innervation on pancreatic function, with variable results[29]. Vagal stimulation modulates both afferent and efferent fibres and both electrical and pharmacological approaches affect multiple metabolically active organs (liver, intestine, muscle, fat). To selectively interrogate the physiological roles of pancreatic parasympathetic efferent nerves, we used our optimized serotype, promoter, titre and delivery route to administer chemogenetic constructs for targeted neural modulation. We delivered the cre-dependent activating hM3d(Gq) chemogenetic construct (AAV-Syn-DIO-hM3D(Gq)-mCherry) using the AAV8 serotype via intraductal infusion (dose 5X) into ChAT-IRES-CRE mice. The construct, labelled by mCherry, was robustly expressed in the cholinergic neurons in the intrapancreatic ganglia (41.75 ± 8.70%) and in a smaller population of neurons projecting to the pancreas from the gastrointestinal tract (8.35 ± 3.7%) (Supplementary Fig. 3c). Vasoactive intestinal peptide and gastrin release peptide were both expressed in subpopulations of mCherry+ intrapancreatic ganglia (Supplementary Fig. 4b). There was no expression in the sympathetic neurons of CG, sensory neurons of NG and DRG (Supplementary Fig. 3a) or pancreatic islets (Supplementary Fig. 4a). Cre-recombinase expression in cholinergic neurons and a cre-dependent construct was sufficient to prevent hepatocyte expression without requiring miR122TS in the construct (Supplementary Fig. 3f). There was no off-target expression (Supplementary Fig. 3c,e). We confirmed clozapine-*N*-oxide (CNO) activation of pancreatic neurons expressing hM3d(Gq) using immunostaining, which demonstrated increased expression of the early immediate gene, cFOS, indicating neural activation (Supplementary Fig. 5a,b) and ex vivo calcium imaging (Supplementary Fig. 5c,d).

Activation of pancreatic cholinergic efferent innervation (Fig. 5a) using CNO substantially reduced basal blood glucose in 6-hour-fasted male mice expressing hM3D(Gq)-mCherry, reducing the area under the curve by 33% (Fig. 5b). Glucose tolerance in ChAT-cre mice expressing cre-dependent hM3D(Gq)-mCherry was substantially improved with a 33% decrease in area under the curve (AUC) compared with control animals injected with AAV8-hSyn-DIO-mCherry (Fig. 5d). Targeted stimulation of pancreatic cholinergic nerves substantially increased plasma insulin before glucose challenge (time 0) and at 10 min after glucose challenge when plasma insulin was almost doubled compared with controls (Fig. 5g). Interestingly, plasma glucagon during glucose tolerance testing was also increased by pancreatic cholinergic nerve activation (Fig. 5h). We next assessed the effects of pancreatic cholinergic nerve stimulation on blood glucose in fasted mice to determine whether the effects of pancreatic cholinergic activation were dependent on ambient glucose concentrations[53]. In overnight fasted mice, there was no effect of CNO activation on basal blood glucose (Fig. 5c). Similarly, pancreatic cholinergic activation did not substantially alter blood glucose or plasma glucagon during insulin tolerance testing (Fig. 5f,i). Neuropeptides such as vasoactive intestinal peptide and gastrin release peptide that are expressed in pancreatic cholinergic neurons can also regulate islet function. To assess the contribution of neuropeptides to improved glucose tolerance with activation of pancreatic cholinergic innervation, we repeated glucose tolerance testing using CNO in the presence of a peripheral muscarinic antagonist, atropine methyl nitrate. Atropine prevented the improvement in glucose tolerance with pancreatic cholinergic activation, suggesting acetylcholine is the major effector (Fig. 5e).

In contrast to the effects in male mice, CNO treatment in female ChAT-cre mice expressing hM3D(Gq)-mCherry or control virus did not substantially alter basal blood glucose, blood glucose during glucose tolerance or insulin tolerance testing, or plasma insulin or glucagon (Extended Data Fig. 4). There was no difference in glucose tolerance in ChAT-cre mice expressing cre-dependent hM3D(Gq)-mCherry compared with those expressing cre-dependent mCherry with vehicle treatment, no difference in glucose tolerance in wild-type (WT) mice treated with CNO or vehicle, and the effects of CNO on basal blood glucose and glucose tolerance were no longer significant 2 and 3 h after administration, respectively (Extended Data Fig. 4).

These data show that selective activation of pancreatic parasympathetic efferent innervation substantially increases plasma insulin and improves glucose tolerance without exacerbating hypoglycaemia in male mice.

Pancreas parasympathetic nerves modify the oral glucose response. To assess whether pancreatic parasympathetic efferent innervation is required for normal glucose tolerance, we examined the effects of targeted ablation of pancreatic cholinergic nerves. We delivered AAV8 with constitutive expression of mCherry and cre-dependent expression of diphtheria toxin A subunit (mCherry-flex-dtA) into the pancreatic tissue of ChAT-IRES-CRE mice (intraductal infusion, dose 5X). Control mice were injected with AAV8 expressing mCherry. Pancreatic parasympathetic VAChT+ innervation was substantially reduced by 78% in mice expressing mCherry-flex-dtA compared with control mice (Fig. 6a,b). Parasympathetic activity is reported to increase in response to feeding and glucose administration, but ablation of pancreatic cholinergic nerves had no effect on blood glucose in fed, 6 h fasted or 16 h fasted mice (Fig. 6c). There was no difference in blood glucose during intraperitoneal (i.p.) glucose tolerance testing between control and dtA treated mice (Fig. 6d). Pancreatic parasympathetic innervation is also activated by oral sensory input to elicit insulin release, a response known as cephalic-phase insulin release. We assessed the effects of targeted ablation of pancreatic cholinergic nerves on the early glucose and insulin response to oral glucose (via licking). Blood glucose was substantially increased within 2 min of oral glucose without insulin release in ChAT-cre mice expressing mCherry-flex-dtA. In control mice, oral glucose increased plasma insulin without a substantial increase in blood glucose (Fig. 6e,f).

Next, we assessed the effects of ablating pancreatic cholinergic innervation on the glucose response to insulin-induced hypoglycaemia and glucopaenia in response to 2 deoxyglucose (2DG), a non-metabolizable glucose analogue. There was no difference in the glucose response to insulin treatment (Fig. 6g); however,

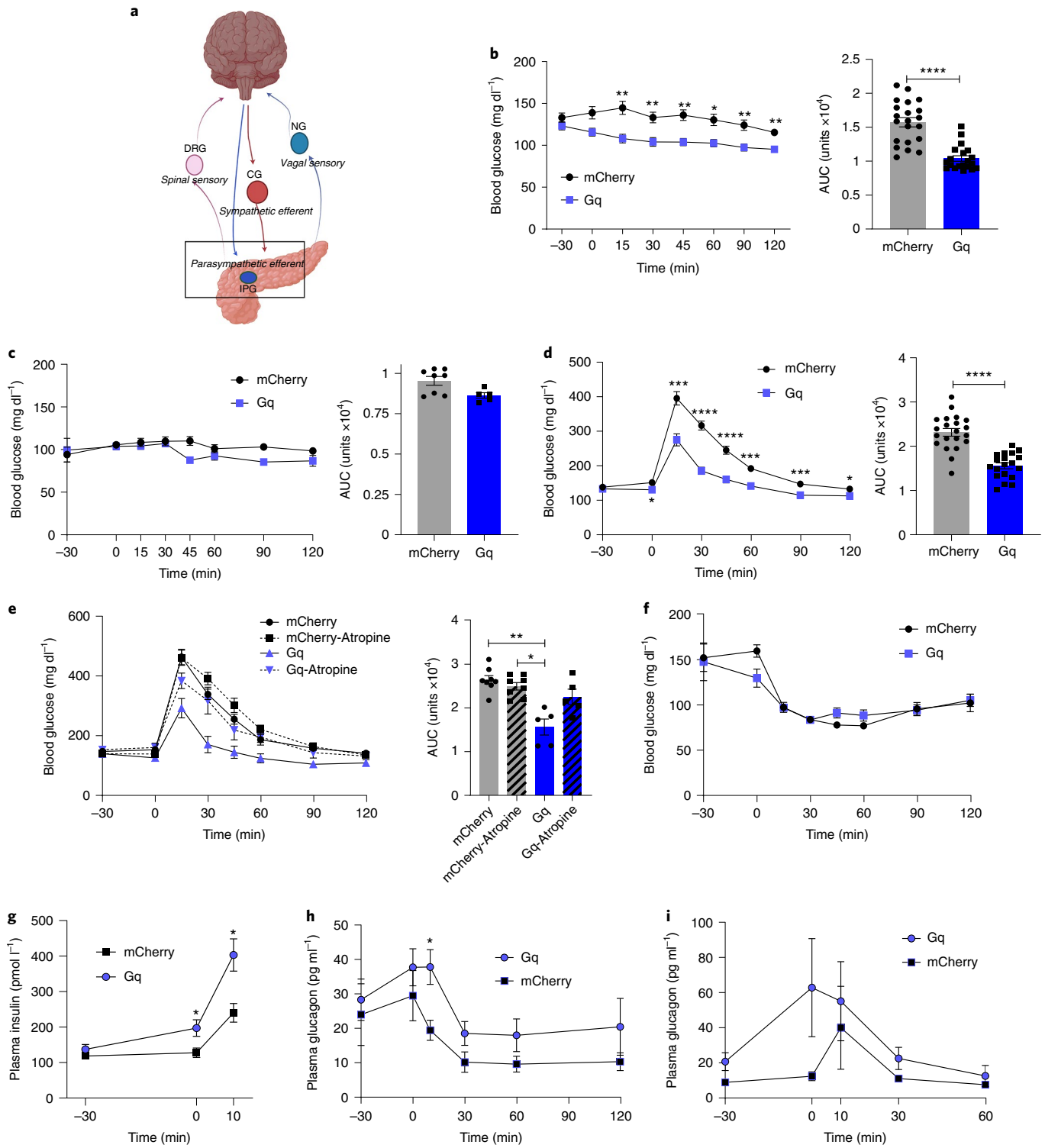

Fig. 5 | Pancreatic parasympathetic activation improves glucose control. a, Schema of parasympathetic intrapancreatic ganglia. **b**, Blood glucose in CNO-treated ChAT-IRES-cre/AAV8-hSyn-DIO-hM3D(Gq)-mCherry and ChAT-IRES-cre/AAV8-hSyn-DIO-mCherry mice (3 mg kg^{-1}, intraperitoneal). After 6 h fasting: right, blood glucose; left, AUC (0 min to 120 min); hM3D(Gq)-mCherry: $n = 22$, mCherry: $n = 21$. **c**, After 16 h fasting: right, blood glucose; left, AUC (0 min to 120 min); hM3D(Gq)-mCherry: $n = 5$, mCherry: $n = 8$. **d**, During glucose tolerance testing (GTT) after 6 h fasting (CNO at −30 min, glucose 2 mg kg^{-1} at 0 min): right, blood glucose; left, AUC (0 min to 120 min); hM3D(Gq)-mCherry: $n = 22$, mCherry: $n = 21$. **e**, During GTT with atropine methyl nitrate (2 mg kg^{-1}, i.p.): right, blood glucose; left, AUC (0 min to 120 min); hM3D(Gq)-mCherry: $n = 5$, mCherry: $n = 8$. **f**, Blood glucose during insulin tolerance testing (ITT) (0.25 U kg^{-1}, i.p.); hM3D(Gq)-mCherry: $n = 5$, mCherry: $n = 8$. **g**, Plasma insulin during GTT at −30, 0 and 10 min; hM3D(Gq)-mCherry: $n = 15$, mCherry: $n = 19$. **h**, Plasma glucagon during GTT at −30, 0, 10, 30, 60 and 90 min; hM3D(Gq)-mCherry: $n = 16$, mCherry: $n = 20$. **i**, Plasma glucagon during ITT at −30, 0, 10, 30 and 60 min; hM3D(Gq)-mCherry: $n = 16$, mCherry: $n = 20$. All data represented as mean ± SEM. Statistical analyses are described in Supplementary Table 2. Figure 5a was created with BioRender.com.

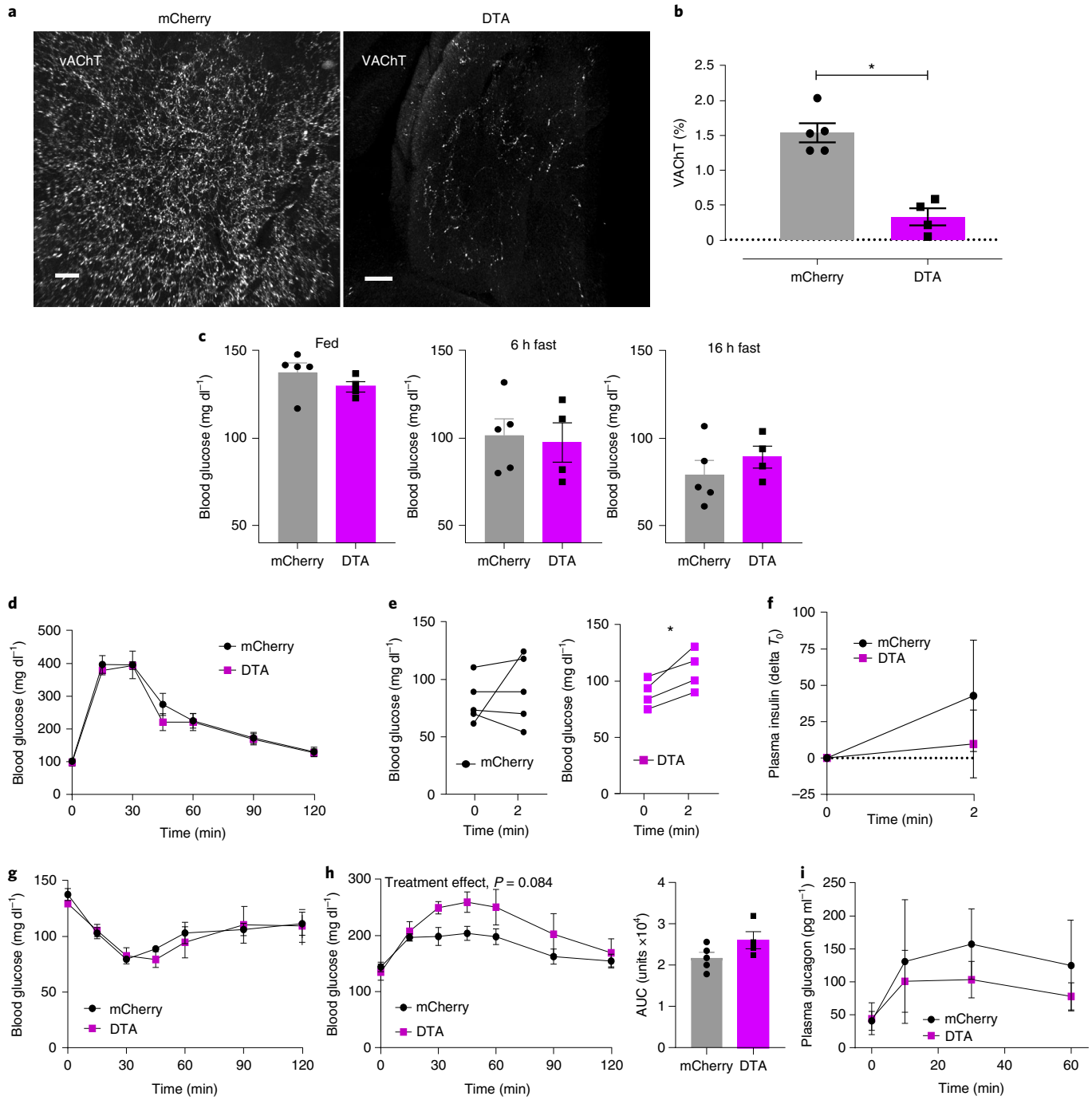

Fig. 6 | Effects of ablation of parasympathetic pancreatic innervation. a, Representative confocal images of iDISCO+ cleared pancreatic parasympathetic innervation (VAChT (white)) 4 weeks after intraductal delivery of AAV8-EF1a-mCherry-flex-dtA or AAV8-EF1a-DIO-mCherry in ChAT-IRES-CRE mice. Scale bars, 100 µm. **b**, Quantification of VAChT+ innervation density, as percentage of total pancreas tissue volume, showing a substantial decrease in parasympathetic innervation in ChAT-DTA mice. **c**, Blood glucose levels of ChAT-DTA and ChAT-mCherry mice in fed (9:00 a.m.), 6 h fasted (3:00 p.m.) and 16 h fasted (9:00 a.m.) states. **d**, Glucose tolerance test (i.p., 2 mg kg^{-1}) in ChAT-DTA ($N=4$) and ChAT-mCherry ($N=5$) mice showing no differences in normal glucose tolerance. **e**, Blood glucose levels are substantially increased within 2 min of oral glucose intake (licking) in ChAT-DTA ($N=4$) in comparison with ChAT-mCherry mice ($N=5$). **f**, Plasma insulin levels before and after 2 min of oral glucose intake in ChAT-DTA ($N=4$) and ChAT-mCherry mice ($N=5$). **g**, Insulin tolerance test (i.p., 0.25 U kg^{-1}) in ChAT-DTA ($N=4$) and ChAT-mCherry ($N=5$) mice showing no differences in blood glucose. **h**, Right: blood glucose levels in response to 2DG (i.p., 200 mg kg^{-1}) in ChAT-DTA ($N=4$) and ChAT-mCherry mice ($N=5$). Left: cumulative change in blood glucose (AUC, 0 min to 120 min). **i**, Plasma glucagon levels in response to 2DG in ChAT-DTA ($N=4$) and ChAT-mCherry mice ($N=5$). All data represented as mean ± SEM. Individual data points represent individual mice. Statistical analyses are described in Supplementary Table 2.

ChAT-cre mice expressing mCherry-flex-dtA had an exaggerated blood glucose response to i.p. 2DG (400 mg kg^{-1}) compared with control mice ($P=0.08$), without substantial changes in glucagon (Fig. 6h,i). Our findings suggest that pancreatic cholinergic nerves may be required for the early insulin response to oral glucose and to restrain the response to glucopaenia.

Pancreas sympathetic activation impairs glucose homoeostasis. Published studies have demonstrated that splanchnic nerve stimulation increases glucagon and suppresses insulin release[27,54,55]. However, this approach modulates pre-ganglionic sympathetic input to the coeliac ganglion and therefore to multiple intra-abdominal organs. Splanchnic nerves also carry sensory afferents from multiple organs[56], hence even in ex vivo studies it is not possible to isolate the effects of efferent sympathetic activation on pancreatic function. To determine the contribution of extrinsic sympathetic ganglia innervating the pancreas to glycaemic control, we used a dual virus approach to specifically activate pancreatic sympathetic efferent neurons. We combined intrapancreatic injection of our optimized serotype AAV8-hSyn-cre-GFP to deliver cre-recombinase to pancreas-projecting neurons in intrapancreatic ganglia and CG, with intracoeliac injection of AAVdj-hSyn-DIO-hM3D(Gq)-mCherry or hSyn-DIO-mCherry to specifically target construct expression to sympathetic pancreas-projecting neurons in the CG. The mCherry-tagged hM3D(Gq) construct was expressed in 1.8% of sympathetic neurons in the CG, which represents 19% of the neurons labelled by delivery of an equivalent titre of AAV8-hSyn-mCherry (Fig. 7b). There was no expression of hM3D(Gq)-mCherry in intrapancreatic ganglia. Activation of pancreatic sympathetic innervation using CNO substantially impaired glucose tolerance, with a 20% increase in AUC compared with control animals injected with AAV8-hSyn-DIO-mCherry, and without effects on basal blood glucose (Fig. 7d). Targeted stimulation of pancreatic sympathetic innervation did not substantially alter blood glucose during insulin tolerance testing. Since a subpopulation of sympathetic neurons project to both pancreas and liver, we assessed the effects of activating pancreas-projecting sympathetic neurons on hepatic gluconeogenesis using a pyruvate tolerance test. There was no difference in blood glucose during pyruvate tolerance test between hM3D(Gq)-mCherry-expressing and control groups with CNO treatment (Fig. 7f), which suggests that the impaired glucose tolerance with activation of pancreatic sympathetic neurons is not mediated by collateral projections to the liver activating gluconeogenesis. There was no significant effect of sympathetic nerve stimulation on plasma insulin or glucagon before or during the glucose challenge compared with controls (Fig. 7g,h). These data support a role of sympathetic pancreatic innervation from the coeliac ganglia in regulating glucose metabolism.

Together, these data demonstrate the feasibility and versatility of optimized AAV delivery of neuromodulatory constructs to pancreatic nerves to elucidate the crucial roles of intrinsic and extrinsic ganglia in pancreatic function (Fig. 8).

Discussion

Our studies used tissue clearing and unbiased quantification to visualize and evaluate neural inputs from extrinsic and intrinsic ganglia to the pancreas. We employed a multilevel approach to achieve optimized gene delivery to afferent or efferent neural circuits innervating the pancreas by combining specific AAV serotypes, tissue-specific promoters and anatomically targeted delivery. MicroRNA (miRNA) target sites can further enhance specificity. Using these methods, we report several presumably previously unreported findings: (1) both CG and intrapancreatic ganglia provide major efferent inputs into the pancreas in mice; (2) distinct neural populations in left and right sensory ganglia innervate the pancreas; (3) AAV serotypes confer specificity for efferent autonomic pancreatic innervation; (4) specific activation of pancreatic parasympathetic cholinergic neurons in intrinsic intrapancreatic ganglia substantially improves glucose tolerance by doubling plasma insulin and (5) targeted activation of pancreatic sympathetic neurons in extrinsic coeliac ganglia substantially impairs glucose tolerance. Our approach provides a method for precise modulation of defined pancreatic nerves to interrogate their roles in metabolic and digestive physiology, and their contribution to pancreatic diseases such as diabetes, pancreatitis and pancreatic cancer.

Several studies using conventional 2D histology and newer 3D tissue-clearing methods have demonstrated that pancreatic tissue is richly innervated. In our studies, we applied tissue clearing and confocal imaging to map the major ganglionic inputs into pancreatic innervation—a straightforward approach that allows quantification across whole ganglia without laborious serial sectioning. This method can readily identify size and 3D distribution, and is particularly suited to the assessment of small scattered structures and their networks, such as intrapancreatic ganglia. We validated our approach by assessing pancreas-innervating ganglia using the retrograde tracer CTβ. Previous studies have examined the contribution of individual pathways to pancreatic innervation in different species; afferent[12] and vagal sensory innervation[57] in mice and sympathetic inputs in rats[14]. Our studies extend these findings by quantifying extrinsic vagal and spinal afferent and sympathetic efferent inputs, and intrinsic intrapancreatic ganglionic inputs in the same animals. The quantification and distribution of CTβ in NG and DRG after intrapancreatic injection are largely in line with published studies[12,57], validating our approach. After CTβ injection, cell bodies in the vagal and spinal sensory ganglia form the majority of labelled neurons. In mice, we identified up to 30% of CG neurons as pancreas-projecting neurons using intraductal delivery of AAV8, a similar proportion seen in previous studies in rats using the fluorescent dye Fast Blue[14]. Unlike the organ-specific organization reported in the stellate ganglion[58], there was no clear regional organization or viscerotopic mapping of pancreatic inputs in the NG, DRG or CG. Interestingly, detailed volume analysis of the CTβ-labelled neurons in sensory ganglia showed marked differences in the labelled populations on the left and right sides. Previous studies have demonstrated distinct roles for left and right gut-innervating nodose populations[59]. Future studies could explore the neurochemical and functional identity of pancreas-innervating neurons in peripheral ganglia, which are currently unknown. Our data confirm the utility of tissue clearing for detailed assessment of ganglionic inputs. Previous work has identified pancreatic nerve remodelling in chronic pancreatitis[35], diabetes[60] and pancreatic cancer[61]. Our detailed mapping can benchmark future studies assessing how the distribution of neural inputs into the pancreas is modified across lifespan, in disease and in response to interventions.

Neural tracing using fluorescent dyes has limitations: (1) there is no neuronal cell type specificity; (2) dyes may have partial anterograde spread; and (3) high fluorescence at injection sites makes it difficult to visualize short-range connections. As a result, we visualized very few CTβ-labelled intrapancreatic ganglia, even with tissue clearing which readily detects intrapancreatic ganglia by immunostaining. Therefore, we decided to map pancreas-innervating ganglia by viral tracing. Viral tools provide several advantages—they are only taken up by nerve terminals and not fibres; high reporter expression provides intense fluorescent labelling; and they can provide cell type-specific retrograde delivery of constructs. AAVs are an attractive option for viral tracing, as they are widely used in the CNS in vivo and provide prolonged expression without eliciting an immune response[46]. Previous studies have employed a variety of methods, such as simple systemic injection[58] or intraganglionic injection[62], to target AAVs to peripheral nerves. However, systemic injection does not provide organ specificity and intraganglionic injection is not feasible for multiple small ganglia dispersed within a specific organ, such as intrapancreatic ganglia. Therefore, we targeted retrograde AAV delivery to the whole pancreas to minimize off-target tissue expression while maximizing transduction to all pancreatic ganglia.

We performed a thorough screen to identify the most appropriate AAV serotypes to identify and quantify expression in the pancreas-projecting ganglia. We found that AAVs 8 and 9 transduced autonomic efferent innervation from extrinsic CG and

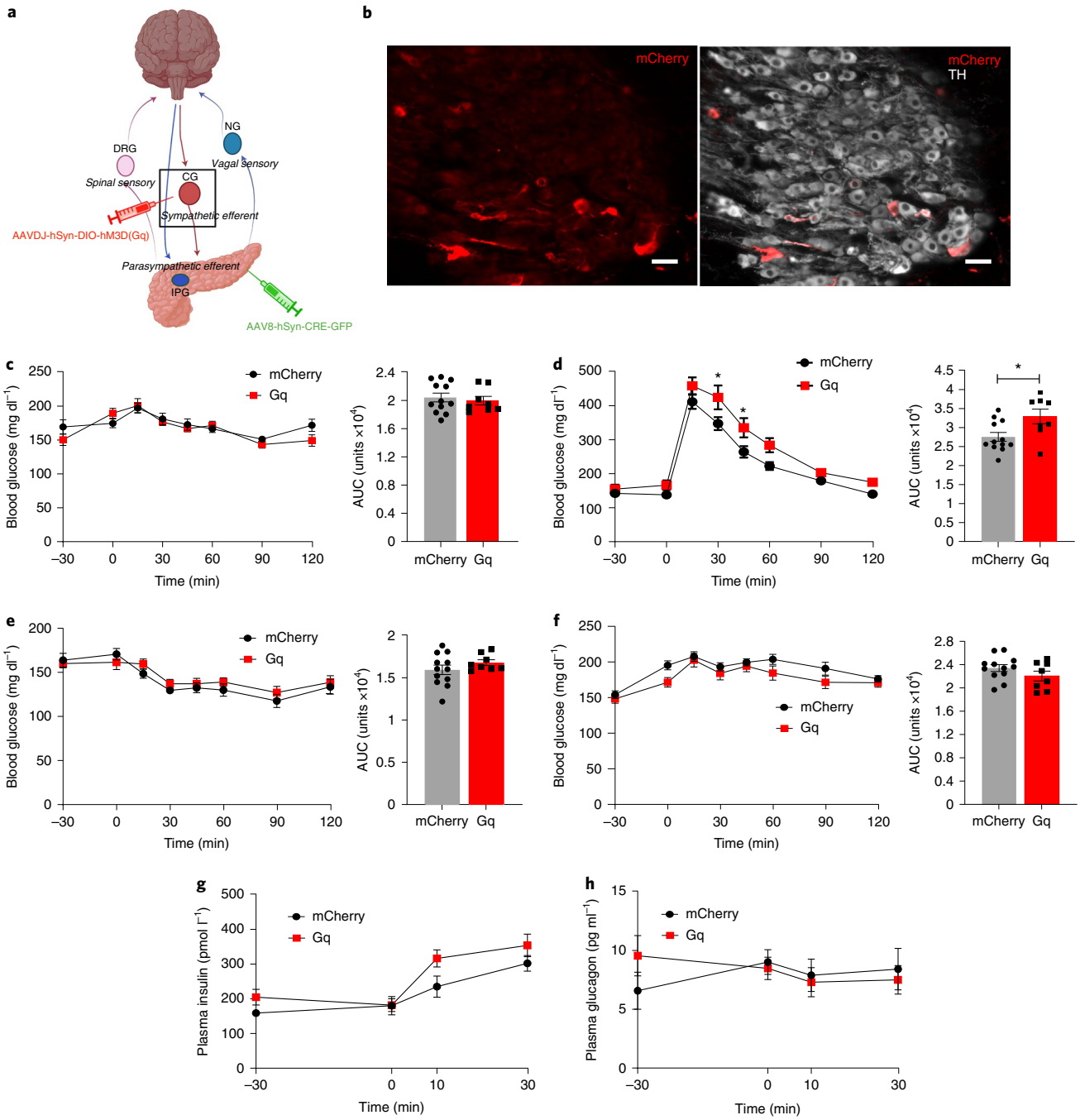

Fig. 7 | Pancreatic sympathetic activation impairs glucose homoeostasis. a, Schema of pancreas-projecting sympathetic neurons in CG. **b**, Images of mCherry expression in sympathetic pancreas-projecting neurons in the CG (TH, white) after intracoeliac injection of AAVdj-hSyn-DIO-hM3D(Gq)-mCherry and intrapancreatic injection of AAV8-hSyn-CRE-eGFP. Scale bar, 50 μm. **c**, Left: blood glucose in CNO-treated (i.p., 3 mg kg^{-1}) AAVdj-hSyn-DIO-hM3D(Gq)-mCherry/AAV8-hSyn-CRE-eGFP mice (N=8) compared to CNO-treated AAV8-hSyn-DIO-mCherry/AAV8-hSyn-CRE-eGFP mice (N=12) after 6 h fasting. Right: cumulative blood glucose change (AUC, 0 min to 120 min). **d**, Left: blood glucose during GTT in CNO-treated (i.p., 3 mg kg^{-1} at −30 min) AAVdj-hSyn-DIO-hM3D(Gq)-mCherry/AAV8-hSyn-CRE-eGFP mice (N=8) compared to CNO-treated AAV8-hSyn-DIO-mCherry/AAV8-hSyn-CRE-eGFP mice (N=12) after 6 h fasting. Right: cumulative blood glucose change (AUC, 0 min to 120 min). **e**, Left: blood glucose during insulin tolerance test (i.p., 0.25 U kg^{-1}) in CNO-treated AAVdj-hSyn-DIO-hM3D(Gq)-mCherry/AAV8-hSyn-CRE-Egfp mice (N=8) compared to CNO-treated AAV8-hSyn-DIO-mCherry/AAV8-hSyn-CRE-eGFP mice (N=12) without fasting. Right: cumulative blood glucose change (AUC, 0 min to 120 min). **f**, Left: blood glucose during pyruvate tolerance test (i.p., 1 g kg^{-1}) in CNO-treated AAVdj-hSyn-DIO-hM3D(Gq)-mCherry/AAV8-hSyn-CRE-eGFP mice (N=8) compared to CNO-treated AAV8-hSyn-DIO-mCherry/AAV8-hSyn-CRE-eGFP mice (N=12) without fasting. Right: cumulative blood glucose change (AUC, 0 min to 120 min). **g**, Plasma insulin during GTT at −30, 0, 10 and 30 min (AAVdj-hSyn-DIO-hM3D(Gq)-mCherry/AAV8-hSyn-CRE-eGFP mice (N=8), AAV8-hSyn-DIO-mCherry/AAV8-hSyn-CRE-Egfp mice (N=12)). **h**, Plasma glucagon during GTT at −30, 0, 10 and 30 min (AAVdj-hSyn-DIO-hM3D(Gq)-mCherry/AAV8-hSyn-CRE-eGFP mice (N=8), AAV8-hSyn-DIO-mCherry/AAV8-hSyn-CRE-Egfp mice (N=9)). All data represented as mean ± SEM. Individual data points represent individual mice. Statistical analyses are described in Supplementary Table 2. Figure 7a was created with BioRender.com.

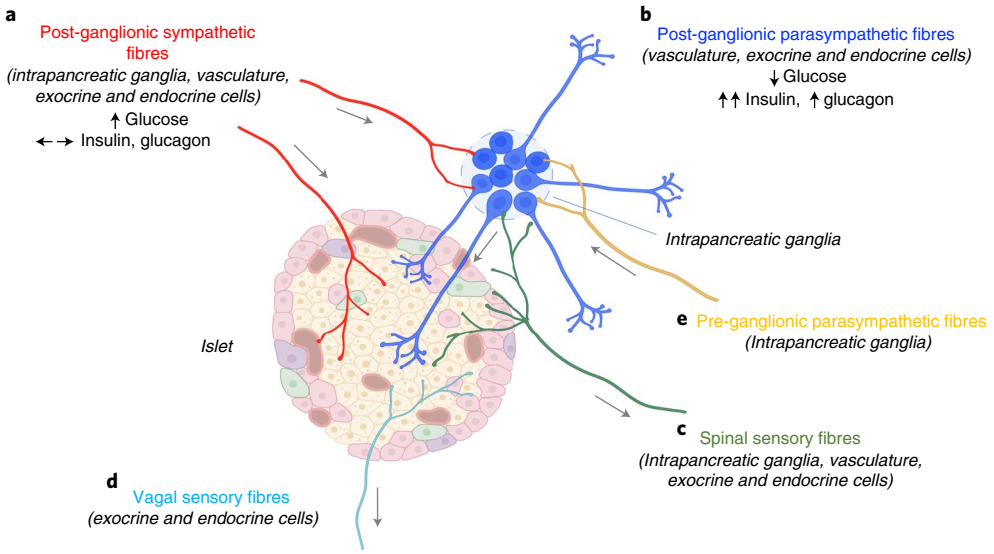

Fig. 8 | Summary of islet innervation. a–d, Islets receive direct innervation from post-ganglionic sympathetic fibres with cell bodies in coeliac ganglia (**a**), post-ganglionic parasympathetic fibres with cell bodies in the intrinsic intrapancreatic ganglia (**b**), spinal sensory fibres with cell bodies in dorsal root ganglia (**c**) and vagal sensory fibres with cell bodies in nodose ganglia (**d**). **e**, Pre-ganglionic parasympathetic fibres, sympathetic and spinal sensory fibres also innervate intrapancreatic ganglia. Chemogenetic activation of intrapancreatic ganglia lowered blood glucose, markedly increased insulin and moderately increased glucagon. Chemogenetic activation of pancreas-projecting sympathetic neurons increased blood glucose without substantial effects on insulin or glucagon. Figure was created with BioRender.com.

intrinsic intrapancreatic ganglia with high efficiency, while AAVrg favoured vagal sensory innervation from NG but with lower efficiency. Even using intraductal delivery of AAV8 at high titres, expression in NG and DRG remained less than 1%. These results confirm that AAV8 is highly selective for autonomic efferent neurons compared with sensory neurons. Interestingly, AAV9/8 have previously been used for retrograde transduction of motor neurons after intralingual injection[63] and sensory neurons after intramuscular injection[40,64] but have not previously been shown to transduce autonomic innervation. Additionally, AAVrg has been used to trace vagal sensory neurons innervating the gut[59]. Consistent with previous studies demonstrating entero-pancreatic neural connections using both retrograde and anterograde tracing, retrograde transport of all AAV serotypes labelled subpopulations of neurons in the gut[18–20]. We also identified mCherry+ fibres in the mesentery with all AAV serotypes. Mesenteric innervation arises from CG, NG and DRG[65], and previous work has shown that the same neurons in peripheral ganglia can project to different organs[66]. Further work is needed to determine whether the same CG neurons project to pancreas and mesentery as seen for neurons with projections to both pancreas and liver. Such findings might suggest an important role for CG neurons in coordinating the neural responses of peripheral organs. The differences in cell types transduced by AAVs 8, 9 and AAVrg suggest that cell-surface receptors used by these serotypes may be differentially expressed on autonomic efferent and afferent neurons. It is possible that this can be exploited further to engineer capsids with even greater specificity for autonomic motor and sensory pathways. However, we did not find an AAV serotype to efficiently transduce DRGs after pancreas delivery. AAVs 6, 8 and 9 have been shown to transduce sensory neurons in the PNS[67] but required direct intraganglionic delivery. Future work could assess whether additional serotypes such as AAV1-Tet1[68], specifically developed for DRG targeting, and AAVPHP.S, an engineered serotype derived from AAV9[69], can effectively target DRG neurons innervating the pancreas.

Many research groups have used intrapancreatic delivery of viral vectors with multiple small-volume injections to target islets[12,70], but intraductal infusion can deliver larger volumes and therefore higher titres of virus, potentially increasing labelling efficiency[47]. We achieved greater CTβ labelling in CG after intraductal infusion compared with intrapancreatic injection, but NG and DRG labelling efficiency were similar using either approach. Intraductal delivery of high titre AAV8 allowed us to optimize expression in CG and improve gene delivery to parasympathetic intrapancreatic ganglia. We found that mCherry+ cell bodies made up almost 30% of intrapancreatic ganglia volume after intraductal delivery of AAV8-hSyn-mCherry. This probably represents a substantial proportion of the neurons in these ganglia. Although the exact cellular composition of intrapancreatic ganglia is unknown, other autonomic and sensory ganglia are composed of several cell types and neurons are only a small proportion of these. For example, neurons are 15% of the total cell population in DRG. These data indicate that parasympathetic intrapancreatic ganglia and sympathetic CG neurons both provide substantial efferent inputs into pancreas innervation.

Viral delivery to peripheral nerves presents more challenges than in the CNS, as peripheral sites have no blood-brain barrier to limit viral spread and are accessible to immune cell-induced reduction in expression. Our longitudinal studies suggest that AAV delivery of mCherry did not elicit apoptosis, and tissue expression was maintained for at least 12 weeks in mice. These findings are in contrast to the expression of green fluorescent protein (GFP) or channelrhodopsin after AAV6 delivery to DRG, which declined after 4 weeks[38]. Although the time course of expression will need to be carefully assessed for each transgene, these results imply that prolonged gene expression may be possible in pancreatic nerves using AAV8.

It is important to ensure no/minimal off-target transgene expression after peripheral virus delivery, as this could alter or confound results. We found minimal expression in spleen or brain after AAV8 or 9 transduction, but both serotypes led to substantial mCherry expression in hepatocytes, irrespective of delivery route and titre. Published studies report that chemogenetic hepatocyte activation increased gluconeogenesis and glycogenolysis to elevate basal blood glucose and impair glucose tolerance, which would confound studies

examining the roles of pancreatic innervation[71,72]. The affinity of AAV8 for hepatocytes has been exploited for construct delivery to the liver using LP-1 promoter with systemic administration[73]. The promoter, hSyn, may be expressed at low levels in liver epithelial cells[74], suggesting the possibility of on-target, off-organ expression with this promoter, but use of the NSE promoter was also insufficient to prevent hepatocyte expression. These findings are in line with results in the CNS where specific promoters have been found to reduce but not completely prevent expression in other cell types[75]. However, combining hSyn promoter-driven mCherry expression with post-transcriptional regulation using multiple tissue-specific miRNA target sites in the 3′ untranslated region (UTR) vastly reduced hepatic expression in vivo. miRNA-122 is expressed abundantly in the liver but not in neural tissue[51] and binding to its target sequence (miR122TS) reduces upstream gene expression via degradation or translational repression[76]. This approach has been applied to reduce gene expression in hepatocytes in vitro and increase cardiac delivery after systemic delivery of AAV9[77] in vivo. Here we show that combining a neuronal specific promoter with miR122TS limited transgene expression to pancreatic nerves in wild-type animals after pancreatic delivery at the titre tested. AAV tropism can change with increasing viral titre[78] and recent studies suggest that interactions between serotype and promoter[79] can also regulate tropism; hence, individual AAV constructs and their titres will need to be assessed for specific expression. Our studies optimizing AAV serotype and titre provide a starting point for these assessments. These results have translational implications as well. Intraductal AAV8 delivery via endoscopic retrograde cholangiopancreatography combined with a neuronal promoter (for example, hSyn or NSE) and translational repression could be used to target gene expression to pancreatic nerves in humans as a therapy for conditions such as pancreatitis or pancreatic cancer, while a ubiquitous promoter such as JeT could transduce both pancreatic tissue and pancreatic innervation.

Our in vivo validation studies show that highly targeted viral delivery of neuromodulatory constructs to pancreatic nerves can be used to evaluate the physiological roles of difficult-to-access neural pathways. Pancreatic parasympathetic cholinergic innervation comprises intrapancreatic ganglia and post-ganglionic fibres in mice and densely innervates pancreatic endocrine tissue. Pancreatic sympathetic innervation from the coeliac ganglia innervates islets, vasculature and intrapancreatic ganglia[80–83]. Viral delivery of chemogenetic constructs allowed us to specifically interrogate the effects of intrinsic intrapancreatic efferent innervation and extrinsic sympathetic innervation on pancreatic endocrine function. Previous studies have relied on systemic administration of cholinergic or adrenergic agonists and antagonists, or assessed the effects of electrical stimulation and/or transection of the vagus or splanchnic nerves on pancreatic function. These studies have led to disparate, often conflicting, results perhaps because these approaches affect multiple intra-abdominal organs and alter both efferent and afferent pathways. In contrast, our viral approach in combination with chemogenetic activation or targeted ablation allowed specific evaluation of pancreatic parasympathetic or sympathetic efferent innervation without effects on other organs or stimulation of afferent nerves. Alternative technologies and delivery methods have been used to assess the roles of autonomic pathways in peripheral organ function, largely using transgenic mice or systemic virus delivery of optogenetic constructs. For example, optogenetic stimulation of channelrhodopsin-2 (ChR2)-expressing neurons in autonomic ganglia after systemic virus administration was used to assess the roles of autonomic ganglia in cardiac function in anaesthetized mice[58]. However, ganglia often innervate multiple organs and this approach does not provide organ specificity. Transgenic expression of ChR2 in sympathetic fibres plus local light delivery has also been used to assess sympathetic fibre contribution to white and brown adipose tissue[84] function; however, transgenic expression would not provide the specificity needed to assess the roles of pancreatic innervation since transgenic neuromodulatory constructs may be expressed in cholinergic fibres in overlying organs. In addition, limited light penetration, the need to fix an optical fibre in a highly mobile region and the risks of pancreatitis make optogenetic regulation of pancreatic innervation a less attractive option, even with the development of wireless and flexible optical fibres[67,85]. On the other hand, combining viral delivery with chemogenetic modulation allows highly targeted regulation in freely moving animals.

Previous pharmacological, nerve stimulation and transection studies demonstrated the importance of neural signals in regulating pancreatic function, but also led to conflicting results. Adrenergic agonists and splanchnic nerve stimulation increased blood glucose in many studies[27,54] but had minimal effect in others[86]. Ex vivo studies, which examined the effects of splanchnic nerve stimulation, also reported conflicting effects on insulin and somatostatin release[27]. These may reflect species differences but might also be a consequence of modulating function across several organs and/or both afferent and efferent fibres. Here, our studies with targeted chemogenetic activation of pancreas-projecting sympathetic innervation impaired blood glucose without substantial effects on pancreatic hormones. Sympathetic innervation is known to target pancreatic vasculature[87,88], hence changes in pancreatic function may be a consequence of altered blood flow. However, while our dual AAV approach achieves specificity, we are able to transduce only a limited number of pancreas-projecting sympathetic neurons. It is possible that there are small changes in pancreatic insulin or glucagon release into the portal circulation that are sufficient to modulate blood glucose but do not substantially alter systemic insulin or glucagon. Further optimization of AAV serotypes and doses may allow greater expression in pancreas-projecting sympathetic neurons.

Similar contradictory findings are also reported for pancreatic parasympathetic function. Pancreatic parasympathetic activity is increased by both high and low blood glucose[89]. Cholinergic agonists increased both plasma insulin and glucagon[90,91]. Vagal stimulation has been reported to increase, decrease or have no effect on blood glucose, insulin secretion[22,31] and glucagon release[22,29]. Similarly, the effects of vagal nerve transection may have no effect or increase blood glucose[34]. In our studies, chemogenetic activation of intrapancreatic cholinergic ganglia consistently lowered blood glucose without hypoglycaemia under basal conditions and, with a glucose challenge, doubled insulin secretion and substantially improved glucose tolerance in vivo. CNO treatment substantially increased plasma insulin even before glucose challenge and augmented the effects of glucose on insulin release, despite lower blood glucose suggesting that parasympathetic efferent activation potentiates glucose-induced insulin secretion. Consistent with this, activation of pancreatic cholinergic efferent nerves had minimal effect on blood glucose in fasted mice or during insulin tolerance testing. While the increase in plasma glucagon with cholinergic efferent stimulation may limit the improvement in glucose tolerance during glucose challenge, it may also minimize the risk of hypoglycaemia, making methods that increase or mimic pancreatic cholinergic activation an attractive approach to improving glucose control. Several neurotransmitters are expressed in intrapancreatic ganglia, including vasoactive intestinal polypeptide, gastrin releasing peptide, pituitary adenylate cyclase-activating polypeptide and acetylcholine[92]. Many studies have pointed to acetylcholine as the main driver of parasympathetic efferent signalling to the Islets of Langerhans[30,53]. However, the roles of other parasympathetic neurotransmitters remain to be clarified. Our findings demonstrating that the effects of parasympathetic efferent activation are lost with atropine pre-treatment are consistent with the dominant role of acetylcholine in regulating insulin release.

In contrast to the effects in male mice, activation of pancreatic parasympathetic efferent nerves had no substantial effect in female mice. Previous studies have reported sex differences in vagal tone. Some reports suggest lower baseline vagal activity[93] and greater response to vagal stimulation in female rats[94], while others report increased vagal activity in females[95]. In our studies, atropine substantially impaired glucose tolerance in female but not in male ChAT-cre mice expressing control virus, suggesting greater parasympathetic activity in female mice during glucose tolerance testing (GTT). Therefore, additional chemogenetic activation may have less effect in females. Additional studies with higher CNO doses may indicate whether it is possible to drive pancreatic parasympathetic activity further to improve glucose tolerance in females.

Further studies are needed to determine the physiological roles of pancreatic cholinergic innervation in the metabolic responses to obesity and in models of diabetes. Our studies suggest that loss of pancreatic cholinergic innervation has minor effects on glycaemic control in mice with normal glucose regulation. Loss of the early insulin response to oral glucose could contribute to impaired post-prandial glucose regulation[96], which we did not detect with glucose measurements in our cohort of freely feeding mice. Cephalic-phase insulin release may play a greater role in glucose regulation in obese individuals[97] and cholinergic innervation could lead to hyperinsulinemia in hyperglycaemic individuals[90]. Targeted ablation of pancreatic cholinergic innervation provides a method to assess its specific contribution to these responses as well as its role in regulating exocrine function and vascular tone.

There is dense cholinergic innervation in mouse islets but the importance of neuronal cholinergic signalling in human islets remains unclear. Two-dimensional histological studies from human pancreatic tissue have identified fewer cholinergic inputs to islets and acetylcholine release from α cells[98]. Functional studies in human islets transplanted into the eye and re-innervated by local circuits have shown little effect on insulin release. However, cholinergic agonists increased activity of hub cells in isolated human islets[99]. Future studies using tissue clearing and 3D imaging in recently isolated human pancreatic tissue and functional studies in pancreatic slice cultures may help clarify the contribution of cholinergic neurons to human metabolic regulation. In addition, further studies are needed to dissect the contribution of pancreatic parasympathetic neurons to digestion, examine the roles of specific neurotransmitters and define the target cells of parasympathetic signalling. Importantly, our current approach provides a method to study the effects of pancreatic nerve activation or inhibition in models of type 1 diabetes and type 2 diabetes as well as exocrine-related diseases such as pancreatic cancer and pancreatitis.

In summary, we have used a combination of tissue clearing, immunostaining and unbiased quantification to map the peripheral ganglia innervating the pancreas. We identified AAV serotypes that preferentially target autonomic efferent nerves in the pancreas. Using a combination of anatomically targeted delivery, tissue-specific promoters and post-translational modification, we achieved precise delivery of transgenes to defined pancreas-projecting neurons. With targeted viral delivery, we demonstrated that specific activation of parasympathetic innervation from intrinsic intrapancreatic ganglia substantially increases insulin release and improves glucose tolerance, while targeted activation of pancreatic sympathetic innervation from extrinsic coeliac ganglia impairs glucose tolerance. These data demonstrate the potential of harnessing pancreatic innervation for metabolic regulation and lay the methodological groundwork for future studies examining the roles of innervation in other peripheral organs. Further studies may clarify the roles of these pancreas-projecting neuronal populations in healthy and diseased states. Our viral approaches directing gene expression to defined pancreatic nerves may allow for the focused examination of the functional roles of pancreatic parasympathetic and sympathetic innervation in glucose metabolism and digestion, and determination of the contribution of pancreatic neural signals to metabolic disease, pancreatic inflammation and malignancy.

Our data have important translational implications. We have shown that viral vectors can be used to precisely target gene expression to pancreatic nerves without Cre-expression, and that the stimulation of pancreatic innervation can substantially improve glucose metabolism. The temporally controlled, reversible regulation of specific pancreatic nerves may also prove useful in the search for novel therapies.

Methods

Viral plasmids and constructs. pAAV-hSyn-mCherry is pAAV-hSyn-hM3D(Gq)-mCherry (Addgene, 50474) with a 1,796 bp deletion of the BamHI fragment containing hM3D(Gq). pAAV-NSE-mCherry was made by amplifying the NSE promoter from pGL3NSE (Addgene, 11606) using primer set oLPNSEIFFor (CTAGGGGTTCCTGCGGCCGCACGCGTGCTAGCTGTATGCAGCTGGACC) and oLPNSEIFRev (TCACCATGGTGGCGACCGGGGGATCCAGATCTCGGTG GTAGTGGCG) and cloning the 1,267 bp PCR product into BamHI/MluI-digested pAAV-hSyn-mCherry in place of the hSyn promoter using the In-Fusion cloning kit (Takara Bio USA) according to the manufacturer's directions. To make pAAV-hSyn-mCherry-miR122, oligos oLPmiR122For (5′-AATTCTTCGCGAACAAA CACCATTGTCACACTCCAGTATACACAAACACCATTGTCACACTCCAC ACGTCACAAACACCATTGTCACACTCCAAGA) and oLPmiR122Rev (5′- AGC TTCTTGGAGTGTGACAATGGTGTTTGTGACGTGTGGAGTGTGACAATG GTGTTTGTGTATACTGGAGTGTGACAATGGTGTTTGTTCGCGAAG) containing three miR122 target sequences to downregulate protein expression in the liver[51] were annealed and ligated to EcoRI/HindII-digested pAAV-hSyn-mCherry.

Preparation of adeno-associated virus. pAAV-hSyn-mCherry and pAAV-hSyn-mCherry-miR122 were packaged into AAV8 as follows: human embryonic kidney cells (HEK293T) (ATCC CRL-3216, mycoplasma testing and short tandem repeat profiling performed by ATCC) were cultured in Dulbecco's modified eagle medium (Gibco, 11965118) supplemented with 10% (v/v) fetal bovine serum (FBS; Gibco, 16000044) and 1% (v/v) penicillin-streptomycin (Gibco, 15140122) at 37 °C in 95% humidified air and 5% CO_2. The plasmid was packaged into AAV8 particles using a calcium phosphate transfection system as described previously[100,101]. Cells were collected and lysed 72 h after transfection. The vector was purified using iodixanol gradient and dialysed against PBS. To titre the purified vector, AAV8 was processed as previously described[100,101] and viral genomes quantified via qPCR using SYBR green chemistry on the AB 7500 FAST real-time PCR platform and primers to the WPRE element: WPRE-For: 5′-GGCT GTTGGGCACTGACAAT-3′; WPRE-Rev: 5′-CTTCTGCTACGTCCCTTCG G-3′. Relative number of full viral particles was calculated using the standard curve method by normalizing to known standard samples.

pAAV-NSE-mCherry and pAAV-hSyn-mCherry were packaged into the following adeno-associated viral serotypes by Virovek: AAV6-hSyn-mCherry, AAV8-hSyn-mCherry, AAV9-hSyn-mCherry and AAV8-NSE-mCherry.

The following adeno-associated viruses were purchased commercially from Addgene: rAAV2-retro-hSyn-mCherry (114472), AAV8-hSyn-DIO-hM3D(Gq)-mCherry (44361), AAV8-hSyn-DIO-mCherry (50459) and AAVrg-hSyn-EGFP (50465).

PRV expressing EGFP (PRV-152) used for retrograde tracing from the pancreas was a generous gift from Lynn Enquist and has been described previously[102]. AAV8-EF1a-mCherry-flex-dtA, AAV8-EF1a-DIO-mCherry, AAV8-hSyn-CRE-eGFP and AAVdj-hSyn-DIO-hM3D(Gq)-mCherry were obtained from the Canadian Neurophotonics Platform Viral Vector Core Facility (RRID:SCR_016477, construct-387, construct-kd2, construct-890 and construct-246, respectively).

In vitro studies. HEK 293T were cultured as described above. Neuro2A (ATCC CCL-131, mycoplasma testing and short tandem repeat profiling performed by ATCC) were cultured in Eagle's minimum essential medium (ATCC, 30–2003) with 10% FBS at 37 °C and 5% CO_2. AML12 cells (ATCC CRL-2254, mycoplasma testing and short tandem repeat profiling performed by ATCC) were cultured in DMEM:F12 medium (ATCC, 30–2006) with 10% FBS at 37 °C and 5% CO_2.

Primary neurons were isolated from dorsal root ganglia of WT C57BL/6J mice (Jackson Laboratories, 000664). Mice were killed and thoracic dorsal root ganglia (5–8 DRGs per animal) were immediately dissected, washed in cold PBS and transferred to Accutase (Gibco, 25–458-CL) for 2 h at r.t. with continuous shaking. Afterwards, DRGs were transferred to primary neuron culture medium: Neurobasal-A (Gibco, 10888-022) supplemented with 10% FBS, B-27 (Gibco, 17504-044), 0.5 mM L-glutamine (Gibco, G7513), 5% normal horse serum (Gibco, 116050-130) and 1% penicillin-streptomycin (Gibco, 15140122). Samples were triturated using flame-polished Pasteur pipettes and incubated in poly-lysine-coated 8-well chambers (Ibidi, 80824). Ciliary neurotrophic factor

(R&D systems, 557-NT/CF) was added every day and cells cultured for 3–5 d before transfection.

Cells were transfected using Fugene (Promega) following the manufacturer's instructions. Briefly, cells were trypsinized and cultured at a density of 4.5×10^5 cells per well in a 24-well plate coated with 5 ug ml^{-1} Fibronectin (ThermoFisher, 33010018). After 24 h, 0.5 µg of plasmid was mixed with Fugene reagent (Promega, E2311) at a 3:1 ratio diluted in OptiMEM (Gibco, 31985-062). Cells were incubated with the mix for 10 min at r.t.

Transfected cells were cultured for 48 h before fixation using 10% paraformaldehyde (Electron Microscopy Sciences, 15710) for 10 min at r.t. Fixed cells were stained with 4′,6-diamidino-2-phenylindole (DAPI) and mounted using Fluoromount mounting media containing DAPI (Southern Biotech, 0100-20).

Fixed cells were imaged using a Zeiss Axio Observer Z.1 microscope at a magnification of ×20. Exposure times and fluorescence intensity were maintained between samples. Image analysis was performed using FIJI[103]. Briefly, images were converted to Tiff format, then made binary. The watershed function was applied to separate particles and cell quantification performed using the 'analyze particle' function. Results are shown as percentage of positive cells (mCherry+) in the total population (DAPI).

Animal studies. WT C57BL/6J, heterozygous ChAT-IRES-Cre female and male mice, and Snap25-2A-GCaMP6s-D on a C57BL/6 background (Jackson Laboratories; 000664, 028861 and 025111, respectively) aged 8–12 weeks were maintained on a temperature controlled environment (20–22 °C, 50–60% humidity) with 12 h of light per day at the Center for Comparative Medicine and Surgery (CCMS) at the Icahn School of Medicine at Mount Sinai (New York, NY, USA), with ad libitum access to food and water. The protocol was reviewed and approved by the Institutional Animal Care and Use Committee of the Icahn School of Medicine at Mount Sinai.

CTβ, AAV6-hSyn-mCherry, AAV8-hSyn-mCherry, AAV9-hSyn-mCherry, AAV8-NSE-mCherry and rAAV retro-hSyn-eGFP were administered to WT C57BL/6J male mice for tracing studies. AAV8-hSyn-DIO-hM3D(Gq)-mCherry, AAV8-hSyn-DIO-mCherry, AAV-EF1a-mCherry-flex-dtA and AAV-EF1a-DIO -mCherry were administered to ChAT-IRES-Cre mice, AAV8-hSyn-CRE-eGFP and AAVdj-hSyn-DIO-hM3D(Gq)-mCherry or AAV8-hSyn-DIO-mCherry were co-administered to WT C57BL/6J male mice (littermates, randomized by body weight to receive either virus) for metabolic studies. AAV-hSyn-hM3D(Gq)-mCherry was administered to Snap25-2A-GCaMP6s-D for calcium imaging studies. Animals receiving misplaced injections or without virus expression were not included in the analysis.

Surgical procedures. Intrapancreatic injections were performed as described previously[12]. Briefly, 10 µl CTβ (Life Technologies, C22841) at 8 µg µl^{-1}, or 1×10^{11} vg (dose 1) or 5×10^{11} vg (dose 2) of AAVs in 5–25 µl PBS were injected in 1 µl increments into random areas of the pancreas of WT C57BL/6J male mice. For intraductal infusions, mice were kept on a liquid diet (Ensure, Abbott laboratories) 1–3 d before surgery. Intraductal infusions were performed as previously described[47]. Briefly, 150 µl CTβ at 0.54 µg µl^{-1} or AAV8 at 1×10^{11} vg (dose 1), 5×10^{11} vg (dose 2), 1×10^{12} vg in 150 µl PBS were infused into the pancreas via cannulation through the duodenum into the hepatopancreatic ampulla and common bile duct at 6 µl min^{-1} using a syringe pump (NE-1000, Syringe ONE, New Era Instruments). For intracoeliac infusions, 2 µl of AAVdj-hSyn-DIO-hM3D(Gq)-mCherry or AAV8-hSyn-DIO-mCherry were administered into the CG at 0.2 µl min^{-1}, using a a Nanofil 36G bevelled needle (NF36BV-2, World Precision Instruments) and Silflex tubing (SILFLEX-2, World Precision Instruments) attached to a Nanofil 10 µl syringe (NANOFIL, World Precision Instruments).

Mice were initially anaesthetized with 3.5% vaporized isoflurane, with the percentage decreased to 1.5–2.5% during the procedures. Mice were kept on a heating pad for the duration of the procedures. Following removal of the canula during intraductal infusion, enrofloxacin (5 mg kg^{-1}, subcutaneous) was administered prophylactically before suturing. Animals were given buprenorphine by intrapancreatic injection (IP; 0.05 mg kg^{-1}) every 12 h for 3 d following surgery. CTβ- and AAV-injected animals were killed at 1 week and 4 weeks post-surgery, respectively, by anaesthetization with 3% isoflurane and perfusion with 10 mg per 100 ml heparinized PBS followed by 4% paraformaldehyde.

Metabolic studies. ChAT-IRES-Cre mice were intraductally infused with AAV8-hSyn-DIO-hM3D(Gq)-mCherry or AAV8-hSyn-DIO-mCherry (control virus), AAV-EF1a-mCherry-flex-dtA or AAV-EF1a-DIO-mCherry. WT C57BL/6J male mice received intracoeliac infusions of AAVdj-hSyn-DIO-hM3D(Gq)-mCherry or AAV8-hSyn-DIO-mCherry and intrapancreatic injections of AAV8-hSyn-CRE-eGFP. Metabolic studies were performed 3 weeks post-surgery, with one test per day. Blood glucose was measured on tail snips using the Contour glucose meter (Bayer, 7097C). Baseline measurements and intraperitoneal glucose tolerance tests (IPGTT) were administered in the afternoon after a 6 h fast. For both tests, clozapine-*N*-oxide (4936, TOCRIS) at 3 mg kg^{-1} in saline/10% DMSO or vehicle (saline/10% DMSO) was administered at time −30 min. For baseline measurements, blood glucose was measured at times −30, 0, 15 and then 30 min intervals to 120 min or 240 min. For IPGTT, 2 g kg^{-1} of D-glucose (Sigma; G8270) in saline was injected at time 0, with blood glucose measured at times −30, 0, 15, 30, 45, 60, 90 and 120 min. Plasma insulin and glucagon were measured on blood collected during the IPGTT studies at time −30 (immediately preceding CNO injection), time 0 (immediately preceding glucose injection) and at 10, 30, 60 and 120 min. For studies that included treatment with peripheral muscarinic antagonist, atropine methyl nitrate (BOC Science), atropine was co-administered with CNO at 2 mg kg^{-1}. For studies on ChAT-IRES-Cre mice expressing the AAV-EF1a-mCherry-flex-dtA and AAV-EF1a-DIO-mCherry (ChAT-DTA and ChAT-mCherry) for parasympathetic innervation ablation, glucopaenia was induced by administering 2-deoxy-glucose (2DG, sigma, D8375) at 200 mg kg^{-1} in the morning (9:00). Insulin tolerance testing (ITT) was performed by injecting insulin (HumulinR, Lilly) at 0.25 U kg^{-1} in fed mice. Plasma glucagon was measured on blood collected during the ITT at time −30 (immediately preceding CNO injection), time 0 (immediately preceding insulin injection), and at 10, 30 and 60 min. Oral glucose experiments were performed in ChAT-DTA and ChAT-mCherry mice. Briefly, mice were food- and water-deprived for 16 h. A solution of 30% sucrose was presented to the mice and they were allowed to lick for 2 min. Blood glucose and plasma insulin were measured at 0 min and 2 min. Pyruvate tolerance test was performed in WT mice expressing AAV8-hSyn-CRE-eGFP/AAVdj-hSyn-DIO-hM3D(Gq)-mCherry and AAV8-hSyn-CRE-eGFP/AAV8-hSyn-DIO-mCherry by injecting sodium pyruvate (Sigma-Aldrich, P5280) at 1 g kg^{-1} (i.p.) in fed mice.

Assays. Blood glucose was determined using a Contour glucometer (Bayer, 7097C). Plasma levels of insulin and glucagon were determined by ELISA (insulin: Mercodia, 10-1247-01, glucagon: 10-1271-01). Plasma glucagon levels are in line with published data using this ELISA[104,105]. SoftMax Pro 7 (Molecular Devices) was utilized for ELISA quantification.

Tissue collection. For all in vivo experiments, the following tissues were collected: CG, NG, DRG (10 and 13, right and left), liver, brain, pancreas, spleen, mesentery, duodenum, kidney, muscle and heart. Tissues were maintained in 4% paraformaldehyde overnight before processing.

Tissue processing for cryosectioning. CG, NG, DRG, brain, spleens and livers were immersed in 30% sucrose (Sigma-Aldrich, 50389) in PBS overnight, then embedded in O.C.T compound (ThermoFisher, 23-730-572), frozen at −80 °C and sectioned at 10 µm thickness. Tissues were stained overnight with mCherry (Abcam, ab205402) + synapsin1 (Cell Signaling, 5297S) or mCherry + tyrosine hydroxylase (TH, Millipore, AB152) at 1:1,000 dilution. Subsequent secondary antibodies used were Alexa Fluor 647 anti-rabbit (Jackson ImmunoResearch, 711-605-152) and Alexa Fluor 594 anti-chicken (Jackson ImmunoResearch, 703-585-155). Tissues were stained with DAPI and coverslipped as stated previously. Samples were visualized using a fluorescent Zeiss Axio Observer Z.1 microscope.

Image analysis was performed using FIJI. To assess mCherry+ expression in brain, liver, spleen, GC, NG and DRG, images were converted to Tiff format, thresholding applied then made binary. The watershed function was applied to separate particles and cell quantification performed using the 'analyze particle' function. Results are shown as percentage of positive cells (mCherry+) in the total population (DAPI) or total number of positive cells. The quantification of mCherry+ overlap with synapsin+ fibres in the liver was done using the JaCOP plugin in FIJI.

Tissue processing for iDISCO+. Pancreata, CG, NG and DRG were processed using the iDISCO+ protocol. Tissues were stained with the following primary antibodies: CTβ (Abcam, ab34992), VAChT (Synaptic Systems, 139103), TH (Millipore, Ab152), somatostasin (SST, R210-01 ImmunoStar), glucagon (SIGMA, G2624), gastrin release peptide (ImmunoStar, 20077) and vasoactive intestinal peptide (ImmunoStar, 20073) at 1:500 dilution; cFOS (Abcam, ab190289) at 1:50 dilution; mCherry (Abcam, ab205402), synapsin1 (Cell Signaling, 5297) and insulin (R&D systems MAB1417) at 1:1,000 dilution. Secondary antibodies used were Alexa Fluor 647 anti-rabbit, Alexa Fluor 546 anti-rabbit, Alexa Fluor 647 anti-chicken, Alexa Fluor 594 anti-mouse (ThermoFisher, A21203) and/or Alexa Fluor 488 anti-guinea pig (ThermoFisher, A11073). All secondary antibodies were diluted 1:1,000, with the exception of cFOS staining (Alexa Fluor 647 anti-rabbit at 1:50 dilution). Ganglia were incubated in primary and secondary antibody for 24 h. Pancreata, previously cut in 0.2–0.5-cm-diameter pieces, were incubated in primary and secondary antibody for 4 d. Tissues were optically cleared using benzyl ether (Sigma, 108014). Samples were visualized in glass-bottom 8-well chambers (Ibidi, 80827) using an inverted Zeiss LSM 780 confocal microscope with a ×10 (NA: 0.3) objective and step size of 5 µm. The total number of neurons was visualized by autofluorescence using the 488/550 nm excitation/emission channel. Expression of CTβ+ or mCherry+ neurons in CG, NG and DRG was quantified using the Spots tool in Imaris.

For the quantification of CTβ and mCherry in intrapancreatic neurons, the Surface tool in Imaris was used to create digital surfaces covering the intrapancreatic ganglia (marked by NF200 staining) and mCherry+ neurons to determine volumes. Volume reconstructions were performed using the Surface tool

with local-contrast background subtraction. Results are shown as percentage of mCherry+ volume per intrapancreatic ganglia volume.

A subset of half pancreata from WT C57BL/6J was cleared and stained for VAChT (Synaptic Systems, 139103) or TH (Millipore, AB152) at a dilution of 1:500 for both. *Z*-stacked optical sections were acquired with an Ultramicroscope II (LaVision BioTec) at ×1.3 magnification and a step size of 3 µm.

Tissue processing for wholemount staining of duodenum and mesentery. Mesentery and duodenum were processed using the following wholemount staining procedure: previously fixed tissues were washed in Tris/NaCl buffer (0.1 M Tris/1.5% NaCl/TX-100 (0.5%)) at room temperature and blocked in Tris/NaCl buffer supplemented with 20% horse serum (Gibco-ThermoFisher, 16050130) for 2 h. Subsequently, primary antibody (synapsin1, dilution 1:500 and mCherry, dilution 1:1,000) prepared in blocking solution was added and samples were incubated at 4 °C for 48 h on an orbital shaker. Tissues were washed in 10% horse serum Tris/NaCl buffer and then incubated in secondary antibody (Alexa Fluor 647 anti-rabbit and Alexa Fluor 594 anti-chicken, dilution 1:1,000) in Tris/NaCl buffer at 4 °C for 48 h on an orbital shaker. Stained tissues were placed in glass-bottom 35 µm dishes (Ibidi, 81158) and confocal imaging was performed using an inverted Zeiss LSM 780 confocal microscope. Quantification was performed using the Imaris Surface tool, as described above.

Statistical analyses. No statistical methods were used to pre-determine sample sizes but our sample sizes are similar to those reported in previous publications[12,14,57].

Data are expressed as means ± s.e.m. Analyses were performed using GraphPad Prism version 8.4.2. Normality was assessed using the Shapiro-Wilk normality test. If normality assumption was met (alpha = 0.05), statistics were performed using Student's unpaired two-tailed *t*-test for comparison between 2 groups, and one-way analysis of variance (ANOVA) with Tukey's post-hoc test for comparison between multiple groups. Two-way repeated measures ANOVA, followed by Sidak's multiple comparison was applied for glucose tolerance tests. If normality was not met, statistics were performed using Mann-Whitney test for comparison between 2 groups and Kruskal-Wallis test followed by Dunn's multiple comparisons test for comparison among multiple groups. $P < 0.05$ was considered significant.

Reporting summary. Further information on research design is available in the Nature Research Reporting Summary linked to this article.

Data availability

The main data supporting the results in this study are available within the paper and its Supplementary Information. The raw and analysed datasets generated during the study are too large to be publicly shared, yet they are available for research purposes from the corresponding author on reasonable request.

Received: 12 June 2020; Accepted: 9 June 2022;
Published online: 14 July 2022

References

1. Grapin-Botton, A. Ductal cells of the pancreas. *Int. J. Biochem. Cell Biol.* **37**, 504–510 (2005).
2. Röder, P. V., Wu, B., Liu, Y. & Han, W. Pancreatic regulation of glucose homeostasis. *Exp. Mol. Med.* **48**, e219 (2016).
3. Guenat, E. et al. Counterregulatory responses to hypoglycemia in patients with glucokinase gene mutations. *Diabetes Metab.* **26**, 377–384 (2000).
4. Thorens, B. Neural regulation of pancreatic islet cell mass and function. *Diabetes Obes. Metab.* **16**, 87–95 (2014).
5. Yamamoto, H., Nagai, K. & Nakagawa, H. Bilateral lesions of the SCN abolish lipolytic and hyperphagic responses to 2DG. *Physiol. Behav.* **32**, 1017–1020 (1984).
6. Begg, D. P. & Woods, S. C. Interactions between the central nervous system and pancreatic islet secretions: a historical perspective. *Adv. Physiol. Educ.* **37**, 53–60 (2013).
7. Holst, J. J. Neural regulation of pancreatic hormone secretion. *Clin. Physiol.* **5**, 34–42 (1985).
8. Tang, S. C. et al. Human pancreatic neuro-insular network in health and fatty infiltration. *Diabetologia* **61**, 168–181 (2018).
9. Butterworth, E. et al. High resolution 3D imaging of the human pancreas neuro-insular network. *J. Vis. Exp.* **2018**, 56859 (2018).
10. Alvarsson, A. et al. A 3D atlas of the dynamic and regional variation of pancreatic innervation in diabetes. *Sci. Adv.* **6**, eaaz9124 (2020).
11. Lindsay, T. H. et al. A quantitative analysis of the sensory and sympathetic innervation of the mouse pancreas. *Neuroscience* **137**, 1417–1426 (2006).
12. Fasanella, K. E., Christianson, J. A., Chanthaphavong, R. S. & Davis, B. M. Distribution and neurochemical identification of pancreatic afferents in the mouse. *J. Comp. Neurol.* **509**, 42–52 (2008).
13. Bou Karam, J. et al. TRPV1 neurons regulate β-cell function in a sex-dependent manner. *Mol. Metab.* **18**, 60–67 (2018).
14. Quinson, N., Robbins, H. L., Clark, M. J. & Furness, J. B. Locations and innervation of cell bodies of sympathetic neurons projecting to the gastrointestinal tract in the rat. *Arch. Histol. Cytol.* **64**, 281–294 (2001).
15. Stagner, J. I. & Samols, E. Role of intrapancreatic ganglia in regulation of periodic insular secretions. *Am. J. Physiol.* **248**, E522–E530 (1985).
16. De Giorgio, R. et al. Patterns of innervation of vasoactive intestinal polypeptide, neuropeptide Y, and gastrin-releasing peptide immunoreactive nerves in the feline pancreas. *Pancreas* **7**, 376–384 (1992).
17. Hoyes, A. D. & Barber, P. Ultrastructure of the perivascular nerve plexuses of the rat pancreas. *Acta Anat.* **108**, 79–88 (1980).
18. Kirchgessner, A. L. & Gershon, M. D. Innervation of the pancreas by neurons in the gut. *J. Neurosci.* **10**, 1626–1642 (1990).
19. Kirchgessner, A. L. & Pintar, J. E. Guinea pig pancreatic ganglia: projections, transmitter content, and the type-specific localization of monoamine oxidase. *J. Comp. Neurol.* **305**, 613–631 (1991).
20. Li, C. et al. Anatomical and functional characterization of a duodeno-pancreatic neural reflex that can induce acute pancreatitis. *Am. J. Physiol. Gastrointest. Liver Physiol.* **304**, 490–500 (2013).
21. Renier, N. et al. iDISCO: a simple, rapid method to immunolabel large tissue samples for volume imaging. *Cell* **159**, 896–910 (2014).
22. Payne, S. C. et al. Differential effects of vagus nerve stimulation strategies on glycemia and pancreatic secretions. *Physiol. Rep.* **8**, 1–11 (2020).
23. Andersson, P. O., Holst, J. & Järhult, J. Effects of adrenergic blockade on the release of insulin, glucagon and somatostatin from the pancreas in response to splanchnic nerve stimulation in cats. *Acta Physiol. Scand.* **116**, 403–409 (1982).
24. Ahrén, B., Veith, R. C. & Taborsky, G. J. J. Sympathetic nerve stimulation versus pancreatic norepinephrine infusion in the dog: 1). Effects on basal release of insulin and glucagon. *Endocrinology* **121**, 323–331 (1987).
25. Barlow, T. E., Greenwell, J. R., Harper, A. A. & Scratcherd, T. The influence of the splanchnic nerves on the external secretion, blood flow and electrical conductance of the cat pancreas. *J. Physiol.* **236**, 421–433 (1974).
26. Fraser, K. A. & Lee, S. S. Autonomic regulation of splanchnic circulation. *Can. J. Gastroenterol.* **5**, 949037 (1991).
27. Kaneto, A., Kajinuma, H. & Kosaka, K. Effect of splanchnic nerve stimulation on glucagon and insulin output in the dog. *Endocrinology* **96**, 143–150 (1975).
28. Roy, M. W., Lee, K. C., Jones, M. S. & Miller, R. E. Neural control of pancreatic insulin and somatostatin secretion. *Endocrinology* **115**, 770–775 (1984).
29. Meyers, E. E., Kronemberger, A., Lira, V., Rahmouni, K. & Stauss, H. M. Contrasting effects of afferent and efferent vagal nerve stimulation on insulin secretion and blood glucose regulation. *Physiol. Rep.* **4**, e12718 (2016).
30. Rodriguez-Diaz, R. et al. Noninvasive in vivo model demonstrating the effects of autonomic innervation on pancreatic islet function. *Proc. Natl Acad. Sci. USA* **109**, 21456–21461 (2012).
31. Stauss, H. M., Stangl, H., Clark, K. C., Kwitek, A. E. & Lira, V. A. Cervical vagal nerve stimulation impairs glucose tolerance and suppresses insulin release in conscious rats. *Physiol. Rep.* **6**, e13953 (2018).
32. Lindskov, J., Amtorp, O. & Rohl Larsen, H. The effects of highly selective vagotomy on exocrine pancreatic function in man. *Gastroenterology* **70**, 545–549 (1976).
33. Smith, R. B., Edwards, J. P. & Johnston, D. Effect of vagotomy on exocrine pancreatic and biliary secretion in man. *Am. J. Surg.* **141**, 40–47 (1981).
34. Fabris, S. E., Thorburn, A., Litchfield, A. & Proietto, J. Effect of parasympathetic denervation of liver and pancreas on glucose kinetics in man. *Metabolism* **45**, 987–991 (1996).
35. Demir, I. E., Friess, H. & Ceyhan, G. O. Neural plasticity in pancreatitis and pancreatic cancer. *Nat. Rev. Gastroenterol. Hepatol.* **12**, 649–659 (2015).
36. Karlsson, S., Sundler, F. & Ahrén, B. Neonatal capsaicin-treatment in mice: effects on pancreatic peptidergic nerves and 2-deoxy-D-glucose-induced insulin and glucagon secretion. *J. Auton. Nerv. Syst.* **39**, 51–59 (1992).
37. Kirkwood, K. S. et al. Substance P inhibits pancreatic exocrine secretion via a neural mechanism. *Am. J. Physiol.* **277**, G314–G320 (1999).
38. Mason, M. R. J. et al. Comparison of AAV serotypes for gene delivery to dorsal root ganglion neurons. *Mol. Ther.* https://doi.org/10.1038/mt.2010.19 (2010).
39. Srivastava, A. In vivo tissue-tropism of adeno-associated viral vectors. *Curr. Opin. Virol.* **21**, 75–80 (2016).
40. Watson, Z. L. et al. Adeno-associated virus vectors efficiently transduce mouse and rabbit sensory neurons coinfected with herpes simplex virus 1 following peripheral inoculation. *J. Virol.* **90**, 7894–7901 (2016).
41. Aviello, G. & D'Agostino, G. Tools for controlling activity of neural circuits can boost gastrointestinal research. *Front. Pharmacol.* **7**, https://doi.org/10.3389/fphar.2016.00043 (2016).
42. Suzuki, H. et al. Characterization of sensory neurons in the dorsal root ganglia of Bax-deficient mice. *Brain Res.* **1362**, 23–31 (2010).

43. Dang, C. H. et al. In vivo dynamics of AAV-mediated gene delivery to sensory neurons of the trigeminal ganglia. *Sci. Rep*. https://doi.org/10.1038/s41598-017-01004-y (2017).
44. Mason, M. R. J. et al. Comparison of AAV serotypes for gene delivery to dorsal root ganglion neurons. *Mol. Ther.* **18**, 715–724 (2010).
45. Geenen, K., Nauwynck, H. J., De Regge, N., Braeckmans, K. & Favoreel, H. W. Brn-3a suppresses pseudorabies virus-induced cell death in sensory neurons. *J. Gen. Virol.* **88**, 743–747 (2007).
46. Jooss, K. & Chirmule, N. Immunity to adenovirus and adeno-associated viral vectors: implications for gene therapy. *Gene Ther.* **10**, 955–963 (2003).
47. Xiao, X. et al. Pancreatic cell tracing, lineage tagging and targeted genetic manipulations in multiple cell types using pancreatic ductal infusion of adeno-associated viral vectors and/or cell-tagging dyes. *Nat. Protoc.* **9**, 2719–2724 (2014).
48. Isgrò, M. A., Bottoni, P. & Scatena, R. Neuron-specific enolase as a biomarker: biochemical and clinical aspects. *Adv. Exp. Med. Biol.* **867**, 125–143 (2015).
49. Kim, J., Adam, R. M., Solomon, K. R. & Freeman, M. R. Involvement of cholesterol-rich lipid rafts in interleukin-6-induced neuroendocrine differentiation of LNCaP prostate cancer cells. *Endocrinology* **145**, 613–619 (2004).
50. Tornoe, J., Kusk, P., Johansen, T. E. & Jensen, P. R. Generation of a synthetic mammalian promoter library by modification of sequences spacing transcription factor binding sites. *Gene* **297**, 21–32 (2002).
51. Lagos-Quintana, M. et al. Identification of tissue-specific microRNAs from mouse. *Curr. Biol.* **12**, 735–739 (2002).
52. Brown, B. D. et al. Endogenous microRNA can be broadly exploited to regulate transgene expression according to tissue, lineage and differentiation state. *Nat. Biotechnol.* **25**, 1457–1467 (2007).
53. Gilon, P. & Henquin, J. C. Mechanisms and physiological significance of the cholinergic control of pancreatic beta-cell function. *Endocr. Rev.* **22**, 565–604 (2001).
54. Brunicardi, F. C. et al. Splanchnic neural regulation of insulin and glucagon secretion in the isolated perfused human pancreas. *Am. J. Surg.* **153**, 34–40 (1987).
55. Bloom, S. R. & Edwards, A. V. The release of pancreatic glucagon and inhibition of insulin in response to stimulation of the sympathetic innervation. *J. Physiol.* **253**, 157–173 (1975).
56. Waxenbaum, J. A. & Varacallo, M. In *StatPearls* (StatPearls Publishing, 2019).
57. Makhmutova, M. et al. Pancreatic β-cells communicate with vagal sensory neurons. *Gastroenterology* **160**, 875–888.e11 (2021).
58. Rajendran, P. S. et al. Identification of peripheral neural circuits that regulate heart rate using optogenetic and viral vector strategies. *Nat. Commun.* **10**, 1944 (2019).
59. Han, W. et al. A neural circuit for gut-induced reward. *Cell* **175**, 887–888 (2018).
60. Lundberg, M. et al. The density of parasympathetic axons is reduced in the exocrine pancreas of individuals recently diagnosed with type 1 diabetes. *PLoS ONE* **12**, e0179911 (2017).
61. Saloman, J. L. et al. Ablation of sensory neurons in a genetic model of pancreatic ductal adenocarcinoma slows initiation and progression of cancer. *Proc. Natl Acad. Sci. USA* **113**, 3078–3083 (2016).
62. Gallaher, Z. R. & Steward, O. Modest enhancement of sensory axon regeneration in the sciatic nerve with conditional co-deletion of PTEN and SOCS3 in the dorsal root ganglia of adult mice. *Exp. Neurol.* **303**, 120–133 (2018).
63. Elmallah, M. K. et al. Sustained correction of motoneuron histopathology following intramuscular delivery of AAV in pompe mice. *Mol. Ther.* **22**, 702–712 (2014).
64. Zheng, H. et al. Efficient retrograde transport of adeno-associated virus type 8 to spinal cord and dorsal root ganglion after vector delivery in muscle. *Hum. Gene Ther.* **21**, 87–97 (2010).
65. Niu, X. et al. Mapping of extrinsic innervation of the gastrointestinal tract in the mouse embryo. *J. Neurosci.* **40**, 6691–6708 (2020).
66. Wee, N. K. Y., Lorenz, M. R., Bekirov, Y., Jacquin, M. F. & Scheller, E. L. Shared autonomic pathways connect bone marrow and peripheral adipose tissues across the central neuraxis. *Front. Endocrinol.* **10**, https://doi.org/10.3389/fendo.2019.00668 (2019).
67. Mickle, A. D. & Gereau, R. W. A bright future? Optogenetics in the periphery for pain research and therapy. *Pain* **159**, S65–S73 (2018).
68. Davis, A. S. et al. Rational design and engineering of a modified adeno-associated virus (AAV1)-based vector system for enhanced retrograde gene delivery. *Neurosurgery* **76**, 216–225 (2015).
69. Chakrabarti, S. et al. Intraarticular adeno-associated virus serotype AAV-PHP.S-mediated chemogenetic targeting of knee-innervating dorsal root ganglion neurons alleviates inflammatory pain in mice. *Arthritis Rheumatol.* **72**, 1749–1758 (2020).
70. Shifrin, A. L., Auricchio, A., Yu, Q.-C., Wilson, J. & Raper, S. E. Adenoviral vector-mediated insulin gene transfer in the mouse pancreas corrects streptozotocin-induced hyperglycemia. *Gene Ther.* **8**, 1480–1489 (2001).
71. Li, J. H. et al. A novel experimental strategy to assess the metabolic effects of selective activation of a Gq-coupled receptor in hepatocytes in vivo. *Endocrinology* **154**, 3539–3551 (2013).
72. Hu, J. et al. A G protein-biased designer G protein-coupled receptor useful for studying the physiological relevance of G q/11-dependent signaling pathways. *J. Biol. Chem.* **291**, 7809–7820 (2016).
73. Nathwani, A. C. et al. Long-term safety and efficacy of factor IX gene therapy in hemophilia B. *N. Engl. J. Med.* **371**, 1994–2004 (2014).
74. Bustos, R. et al. Synapsin I is expressed in epithelial cells: localization to a unique trans-Golgi compartment. *J. Cell Sci.* **114**, 3695–3704 (2001).
75. Rolland, A.-S., Kareva, T., Kholodilov, N. & Burke, R. E. A quantitative evaluation of a 2.5-kb rat tyrosine hydroxylase promoter to target expression in ventral mesencephalic dopamine neurons in vivo. *Neuroscience* **346**, 126–134 (2017).
76. Bandiera, S., Pfeffer, S., Baumert, T. F. & Zeisel, M. B. miR-122–a key factor and therapeutic target in liver disease. *J. Hepatol.* **62**, 448–457 (2015).
77. Qiao, C. et al. Liver-specific microRNA-122 target sequences incorporated in AAV vectors efficiently inhibits transgene expression in the liver. *Gene Ther.* **18**, 403–410 (2011).
78. Mcmaster, M. L., Kristinsson, S. Y., Turesson, I., Bjorkholm, M. & Landgren, O. Preferential labeling of inhibitory and excitatory cortical neurons by endogenous tropism of AAV and lentiviral vectors. *Clin. Lymphoma* **9**, 19–22 (2010).
79. Powell, S. K., Samulski, R. J. & McCown, T. J. AAV capsid-promoter interactions determine CNS cell-selective gene expression in vivo. *Mol. Ther.* **28**, 1373–1380 (2020).
80. Chiu, Y.-C., Hua, T.-E., Fu, Y.-Y., Pasricha, P. J. & Tang, S.-C. 3-D imaging and illustration of the perfusive mouse islet sympathetic innervation and its remodelling in injury. *Diabetologia* **55**, 3252–3261 (2012).
81. Klein, E., Salinas, A., Shemesh, E. & Dreiling, D. A. Effects of autonomic denervation on canine exocrine pancreatic secretion and blood flow. *Int. J. Pancreatol.* **3**, 165–170 (1988).
82. RICHINS, C. A. Effect of sympathetic nerve stimulation on blood flow and secretion in the pancreas of the cat. *Am. J. Physiol.* **173**, 467–470 (1953).
83. Mei, Q., Mundinger, T. O., Lernmark, K. & Taborsky, G. J. J. Increased galanin expression in the celiac ganglion of BB diabetic rats. *Neuropeptides* **40**, 1–10 (2006).
84. Zeng, W. et al. Sympathetic neuro-adipose connections mediate leptin-driven lipolysis. *Cell* **163**, 84–94 (2015).
85. Spencer, N. J. et al. Identification of a rhythmic firing pattern in the enteric nervous system that generates rhythmic electrical activity in smooth muscle. *J. Neurosci.* **38**, 5507–5522 (2018).
86. Bloom, S. R., Edwards, A. V. & Vaughan, N. J. The role of the autonomic innervation in the control of glucagon release during hypoglycaemia in the calf. *J. Physiol.* **236**, 611–623 (1974).
87. Tang, S.-C., Peng, S.-J. & Chien, H.-J. Imaging of the islet neural network. *Diabetes Obes. Metab.* **16**, 77–86 (2014).
88. Rodriguez-Diaz, R. et al. Innervation patterns of autonomic axons in the human endocrine pancreas. *Cell Metab.* **14**, 45–54 (2011).
89. Banarer, S., McGregor, V. P. & Cryer, P. E. Intraislet hyperinsulinemia prevents the glucagon response to hypoglycemia despite an intact autonomic response. *Diabetes* **51**, 958–965 (2002).
90. Teff, K. L. & Townsend, R. R. Prolonged mild hyperglycemia induces vagally mediated compensatory increase in C-peptide secretion in humans. *J. Clin. Endocrinol. Metab.* **89**, 5606–5613 (2004).
91. Ahrén, B., Stern, J. S., Gingerich, R. L., Curry, D. L. & Havel, P. J. Glucagon secretory response to hypoglycaemia, adrenaline and carbachol in streptozotocin-diabetic rats. *Acta Physiol. Scand.* **155**, 215–221 (1995).
92. Ahrén, B., Wierup, N. & Sundler, F. Neuropeptides and the regulation of islet function. *Diabetes* **55**, S98–S107 (2006).
93. Khasar, S. G. et al. Gender and gonadal hormone effects on vagal modulation of tonic nociception. *J. Pain.* **2**, 91–100 (2001).
94. Du, X. J., Dart, A. M. & Riemersma, R. A. Sex differences in the parasympathetic nerve control of rat heart. *Clin. Exp. Pharmacol. Physiol.* **21**, 485–493 (1994).
95. Saleh, T. M. & Connell, B. J. 17β-Estradiol modulates baroreflex sensitivity and autonomic tone of female rats. *J. Auton. Nerv. Syst.* **80**, 148–161 (2000).
96. Teff, K. L. How neural mediation of anticipatory and compensatory insulin release helps us tolerate food. *Physiol. Behav.* **103**, 44–50 (2011).
97. Teff, K. L. & Townsend, R. R. Early phase insulin infusion and muscarinic blockade in obese and lean subjects. *Am. J. Physiol.* **277**, R198–208 (1999).
98. Rodriguez-Diaz, R. et al. Alpha cells secrete acetylcholine as a non-neuronal paracrine signal priming beta cell function in humans. *Nat. Med.* **17**, 888–892 (2011).
99. Johnston, N. R. et al. Beta cell hubs dictate pancreatic islet responses to glucose. *Cell Metab.* **24**, 389–401 (2016).

100. Morgenstern, P. F., Marongiu, R., Musatov, S. A. & Kaplitt, M. G. Adeno-associated viral gene delivery in neurodegenerative disease. *Methods Mol. Biol.* **793**, 443–455 (2011).
101. Marongiu, R. et al. Gene therapy blockade of dorsal striatal p11 improves motor function and dyskinesia in parkinsonian mice. *Proc. Natl Acad. Sci. USA* **113**, 1423–1428 (2016).
102. Smith, B. N. et al. Pseudorabies virus expressing enhanced green fluorescent protein: a tool for in vitro electrophysiological analysis of transsynaptically labeled neurons in identified central nervous system circuits. *Proc. Natl Acad. Sci. USA* **97**, 9264–9269 (2000).
103. Schneider, C. A., Rasband, W. S. & Eliceiri, K. W. NIH Image to ImageJ: 25 years of image analysis. *Nat. Methods* **9**, 671–675 (2012).
104. Capozzi, M. E. et al. The limited role of glucagon for ketogenesis during fasting or in response to SGLT2 inhibition. *Diabetes* **69**, 882–892 (2020).
105. Wewer Albrechtsen, N. J. et al. Dynamics of glucagon secretion in mice and rats revealed using a validated sandwich ELISA for small sample volumes. *Am. J. Physiol. Endocrinol. Metab.* **311**, E302–E309 (2016).

Acknowledgements

We thank J. Friedman for critical comments; N. Tzavaras, E. Agullo-Pascual and D. Benson from the Bioimaging Resource Center for assistance and support; G. Gittes and members of the Gittes lab for assistance with intraductal pancreatic surgeries and A. Caicedo and members of the Caicedo lab for advice on intraductal pancreatic surgeries. A.A. was supported by a senior postdoctoral fellowship from the Charles H. Revson Foundation (Grant No. 18-25) and a postdoctoral scholarship from the Swedish Society for Medical Research (SSMF). R.F.H. was supported in part by NIH Training Grant T32GM007280 and F31DK129016. M.J.-G. was supported in part by the Naomi Berries Diabetes Center Russell Berrie Foundation Award. This work was supported by the American Diabetes Association Pathway to Stop Diabetes Grant ADA No. 1-17-ACE-31 and in part by grants from the National Institutes of Health (R01NS097184, OT2OD024912, R01DK124461), the Department of Defense (W81XWH-20-1-0345 and Discovery Award No. W81XWH-20-1-0156) and by funding to M.G.K. from the JPB Foundation. We also thank the NIDDK-supported Einstein-Sinai Diabetes Research Center (DRC) (P-30 DK020541).

Author contributions

M.J.-G., R.L. and L.E.P. performed experiments, analysed data and contributed to the writing of the manuscript. A.A., R.M. and R.F.H. performed experiments and reviewed the manuscript. M.G.K., R.C.V. and G.J.S. provided experimental and intellectual expertise. S.A.S. performed experiments, analysed data and wrote the manuscript. M.J.-G., R.L., L.E.P. and S.A.S. designed the studies. All authors discussed the results and edited the manuscript.

Competing interests

S.A.S is a named inventor of the patent 'Compositions and methods to modulate cell activity' (US9399063B2). S.A.S. and M.G.K. are co-founders of Redpin Therapeutics, and consult for and have equity in the company. M.G.K. also consults for Meira GTx. All other authors declare no competing interests.

Additional information

Extended data is available for this paper at https://doi.org/10.1038/s41551-022-00909-y.

Supplementary information The online version contains supplementary material available at https://doi.org/10.1038/s41551-022-00909-y.

Correspondence and requests for materials should be addressed to S. A. Stanley.

Peer review information *Nature Biomedical Engineering* thanks Philipe Blancou, Gordon Weir and the other, anonymous, reviewer(s) for their contribution to the peer review of this work.

Reprints and permissions information is available at www.nature.com/reprints.

Publisher's note Springer Nature remains neutral with regard to jurisdictional claims in published maps and institutional affiliations.

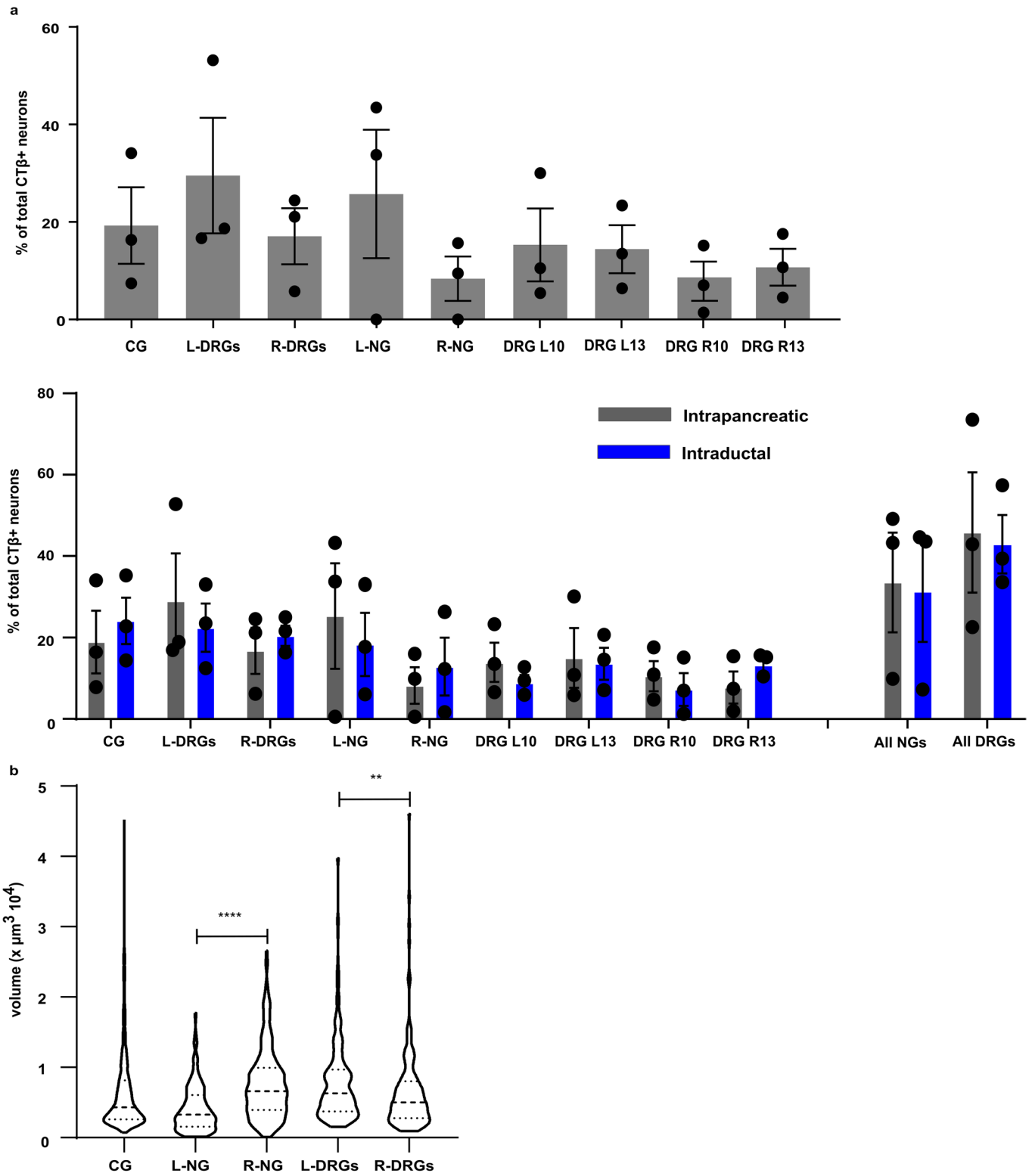

Extended Data Fig. 1 | Distribution of CTβ + pancreas-innervating neurons across ganglia. a) Distribution of CTβ + pancreas-innervating neurons between ganglia (number of CTβ + pancreas-innervating neurons in specified ganglia/total number of CTβ + pancreas-innervating neurons in all ganglia) using intrapancreatic injection (IP, grey bars, upper panel) and comparison with intraductal infusion (ID, blue bars). N = 3 mice/ ganglia. **b)** Size distribution of CTβ + pancreas-innervating neurons in ganglia. Statistical analyses are described in Supplementary Table 3.

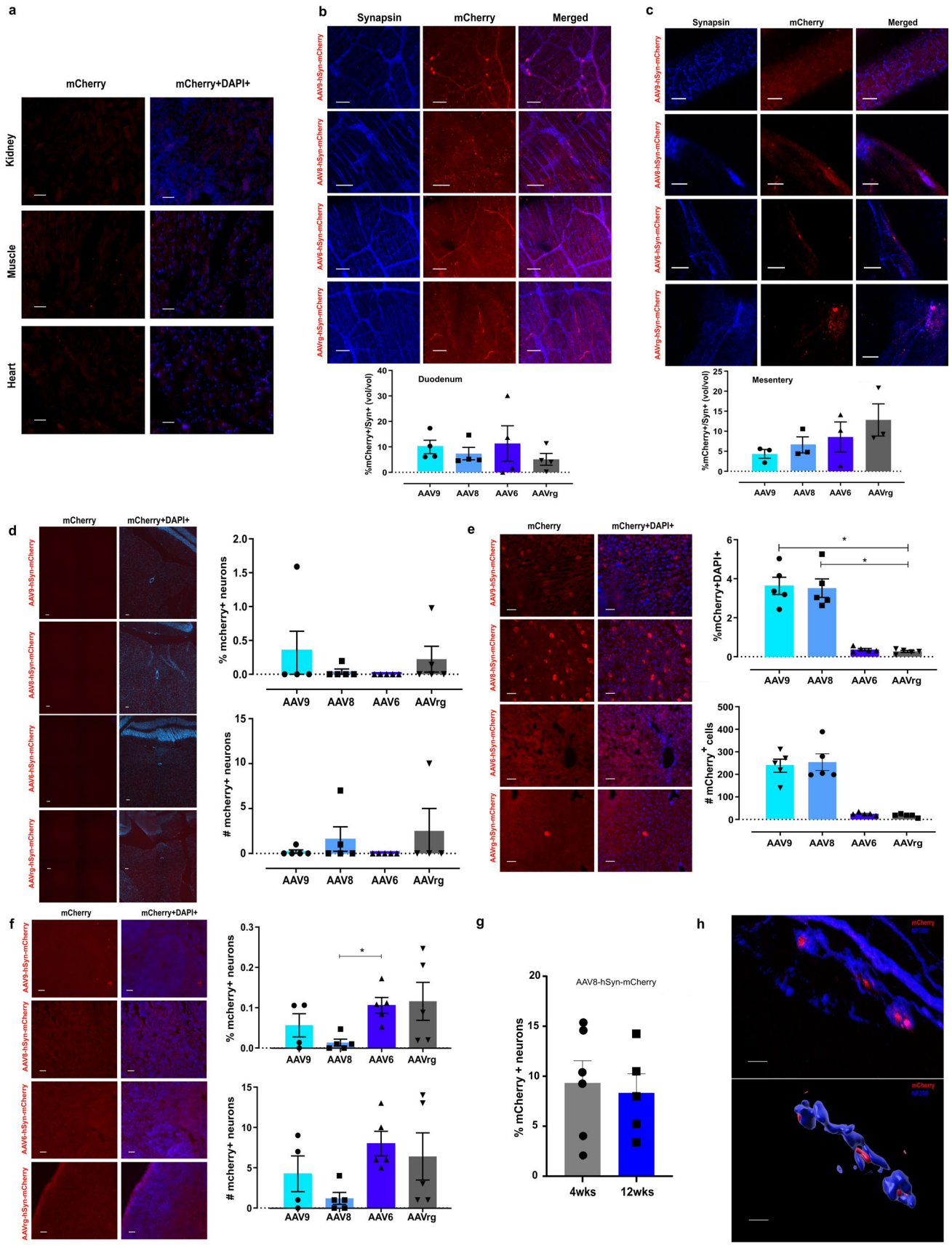

Extended Data Fig. 2 | See next page for caption.

Extended Data Fig. 2 | Off-target expression after intrapancreatic delivery of AAV. a) Off-target mCherry expression in kidney, muscle and heart, 4 weeks after intrapancreatic AAV8-hSyn-mCherry injection. Scale bars: 50 μm. **b)** Expression of mCherry 4 weeks after intrapancreatic injection of AAV8-hSyn-mCherry injection (serotypes 6, 8, 9 and rg). **c)** Images of mCherry and Synapsin in enteric nerves (duodenum). Scale bars: 100 μm. Quantification of viral expression as mCherry+ volume within Synapsin+ volume (bottom panel). n = 4 mice/group. **d)** Images of mCherry and Synapsin in mesenteric fibers. Scale bars: 50 μm. Quantification of mCherry+ volume within Synapsin+ volume in mesentery (bottom panel). n = 3 mice/group. **e)** Images of hindbrain stained for mCherry. Scale bars: 100 μm. Right panel: mCherry+ expression as percentage (upper) and total number (lower), n = 5 mice/group. **f)** Images of mCherry in liver. Scale bars: 50 μm. Right panel: expression of mCherry+ cells as percentage (upper) and total number (lower), n = 5 mice/group. **g)** Images of mCherry in spleen. Scale bars: 50 μm. Right: expression of mCherry+ cells as percentage (upper) and total number (lower), n = 5 mice/group. **h)** Quantification of mCherry+ neurons in CG, 4 (N = 6 mice) and 12 (N = 5 mice) weeks after intrapancreatic injection of AAV8-hSyn-mCherry, $1*10^{11}$ vg. **i)** Confocal images (left) and 3D volume segmentation analysis (right) of mCherry + /NF200 + intrapancreatic ganglia after intrapancreatic delivery of AAV8-hsyn-mCherry. N = 88 ganglia from 20 mice in 5 independent studies. Scale bar: 30 μm. Statistical analyses are described in Supplementary Table 3.

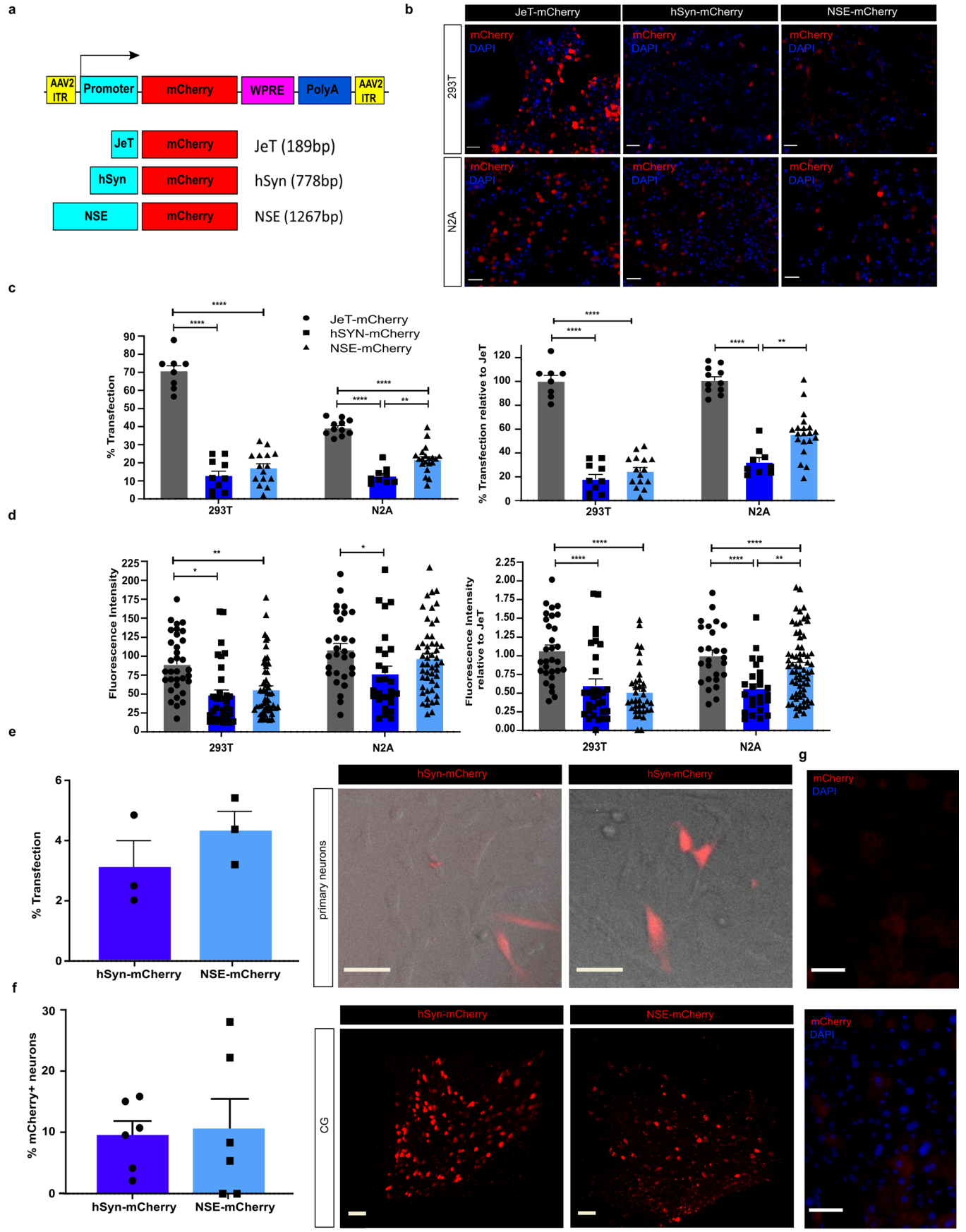

Extended Data Fig. 3 | See next page for caption.

Extended Data Fig. 3 | Neuronal specific promoters for gene delivery into pancreatic innervation. a) Schematic representation of AAV plasmid constructs. **b)** Immunofluorescence images of HEK293T and Neuro2A cells after transfection with pJeT-mCherry, phSyn-mCherry and pNSE-mCherry. Scale bars: 50 μm. **c)** Percentage of total cells (left) or percentage of relative to JeT-mcherry expressing mCherry+ cells in HEK293T and N2A after transfection with pJet-mCherry, phSyn-mCherry and pNSE-mCherry. N = 3 independent experiments. **d)** Fluorescence intensity of mCherry + (left) or relative to JeT-mCherry in HEK293T and N2A after transfection with pJet-mCherry, phSyn-mCherry and pNSE-mCherry. N = 3 independent experiments. **e)** Quantification of mCherry expression in primary DRG neurons after transfection with phSyn-mCherry and pNSE-mCherry (left panel) and fluorescence/transmitted light images (middle and right panels) showing mCherry (red). Scale bar: 25 μm. N = 3 independent experiments. **f)** Percentage of CG neurons expressing mCherry+ after intrapancreatic injection of AAV8-hSyn-mCherry and AAV8-NSE-mCherry (left panel) and corresponding images of iDISCO+ cleared CG (middle and right panels). Scale bars: 100 μm. N = 6 samples/group. **g)** Immunofluorescence image of mCherry expression in liver after intrapancreatic injection of AAV8-NSE-mCherry. Scale bars: 50 μm. Statistical analyses are described in Supplementary Table 3.

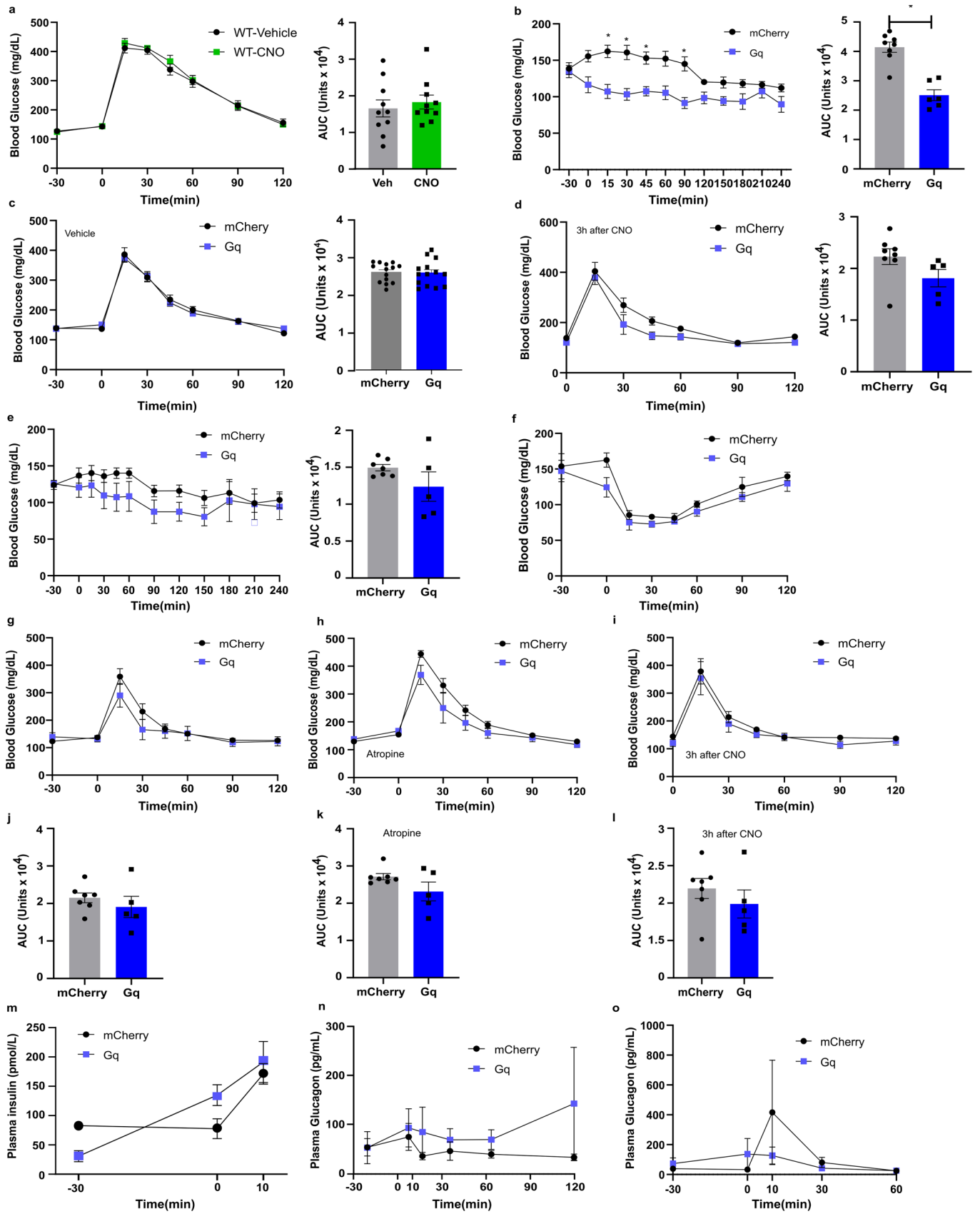

Extended Data Fig. 4 | See next page for caption.

Extended Data Fig. 4 | CNO does not affect GTT in wild-type (WT) mice and female ChAT-IRES-cre/AAV8-Syn-DIO-hM3D(Gq)-mCherry. a) GTT in WT mice with CNO (ip, 3 mg/kg) or vehicle (10%DMSO). Right: Cumulative blood glucose change (AUC, 0′ to 120′). N = 10. Blood glucose in male ChAT-IRES-cre/AAV8-Syn-DIO-hM3D(Gq)-mCherry (N = 5) and ChAT-IRES-cre/AAV8-hSyn-DIO-mCherry (N = 8). **b)** After 6 h fasted with CNO treatment (3 mg/kg ip) over 240 mins. Right: cumulative blood glucose change (AUC, 0′ to 240′). **c)** During GTT after 6 h fast (vehicle at -30min, glucose 2 mg/kg at 0 min). Right: cumulative blood glucose change (AUC, 0′ to 120′). **d)** During GTT after 6 h fast (CNO at -180min, glucose 2 mg/kg at 0 min). Right: cumulative blood glucose change (AUC, 0′ to 120′). Blood glucose in female CNO-treated ChAT-IRES-cre/AAV8-hSyn-DIO-hM3D(Gq)-mCherry (N = 5) and ChAT-IRES-cre/AAV8-hSyn-DIO-mCherry (n = 7) mice (CNO: 3 mg/kg, intraperitoneal). **e)** After 6 h fast. Right: cumulative blood glucose change (AUC, 0′ to 120′). **f)** During ITT (CNO at -30min, Insulin 0.25U/kg i.p. at 0 min). **g)** During GTT after 6 h fast (CNO at -30min, glucose 2 mg/kg at 0 min). **h)** During GTT with atropine methyl nitrate (2 mg/kg, i.p.). **i)** During GTT after 6 h fast (CNO at -180min, glucose 2 mg/kg at 0 min). **j)** Cumulative blood glucose change (AUC, 0′ to 120′) during GTT. **k)** Cumulative blood glucose change (AUC, 0′ to 120′) during GTT with atropine**. l)** Cumulative blood glucose change (AUC, 0′ to 120′) during GTT 180 mins after CNO. **m)** Plasma insulin during GTT at -30, 0, and 10 mins. **n)** Plasma glucagon during GTT at -30, 0, 10, 30, 60 and 90 mins. **o)** Plasma glucagon during ITT at -30, 0, 10, 30, and 60 mins. Statistical analyses are described in Supplementary Table 3.

nature portfolio

Corresponding author(s): Sarah Stanley

Last updated by author(s): Jun 1, 2022

Reporting Summary

Nature Portfolio wishes to improve the reproducibility of the work that we publish. This form provides structure for consistency and transparency in reporting. For further information on Nature Portfolio policies, see our Editorial Policies and the Editorial Policy Checklist.

Statistics

For all statistical analyses, confirm that the following items are present in the figure legend, table legend, main text, or Methods section.

n/a	Confirmed
☐	☒ The exact sample size (*n*) for each experimental group/condition, given as a discrete number and unit of measurement
☐	☒ A statement on whether measurements were taken from distinct samples or whether the same sample was measured repeatedly
☐	☒ The statistical test(s) used AND whether they are one- or two-sided *Only common tests should be described solely by name; describe more complex techniques in the Methods section.*
☒	☐ A description of all covariates tested
☐	☒ A description of any assumptions or corrections, such as tests of normality and adjustment for multiple comparisons
☐	☒ A full description of the statistical parameters including central tendency (e.g. means) or other basic estimates (e.g. regression coefficient) AND variation (e.g. standard deviation) or associated estimates of uncertainty (e.g. confidence intervals)
☐	☒ For null hypothesis testing, the test statistic (e.g. *F*, *t*, *r*) with confidence intervals, effect sizes, degrees of freedom and *P* value noted *Give P values as exact values whenever suitable.*
☒	☐ For Bayesian analysis, information on the choice of priors and Markov chain Monte Carlo settings
☒	☐ For hierarchical and complex designs, identification of the appropriate level for tests and full reporting of outcomes
☒	☐ Estimates of effect sizes (e.g. Cohen's *d*, Pearson's *r*), indicating how they were calculated

Our web collection on statistics for biologists contains articles on many of the points above.

Software and code

Policy information about availability of computer code

Data collection	A Zeiss Axio Observer Z.1 microscope and an inverted Zeiss LSM 780 confocal microscope were used for immunofluorescence imaging and iDISCO-cleared small tissues. An ultramicroscope II (LaVision BioTec, Bielefeld, Germany) was used for iDISCO-cleared pancreas. SpectraMax i3X, Molecular Devices, was used for ELISA detection. A Bayer Contour Glucometer was used to obtain blood-glucose values.
Data analysis	GraphPad Prism 8 software R (ver.8.4.2) was used for statistical analysis and graphic plotting. ImageJ (ver 1.52P) was used for transfection analysis (using the 'Analyze Particle function') and dual pancreas/liver transduction (JaCOP plugin). Imaris Software, Bitplane, ver.9.31-6.5.1 was used for 3D imaging segmentation (using 'Surface Tool' and 'Sports Tool'), analysis and video preparation. SoftMax Pro 7.0 was used for ELISA quantification.

For manuscripts utilizing custom algorithms or software that are central to the research but not yet described in published literature, software must be made available to editors and reviewers. We strongly encourage code deposition in a community repository (e.g. GitHub). See the Nature Portfolio guidelines for submitting code & software for further information.

Data

Policy information about availability of data

All manuscripts must include a data availability statement. This statement should provide the following information, where applicable:

- Accession codes, unique identifiers, or web links for publicly available datasets
- A description of any restrictions on data availability
- For clinical datasets or third party data, please ensure that the statement adheres to our policy

The main data supporting the findings of this study are available within the paper and its Supplementary Information. The raw and analysed datasets generated during the study are too large to be publicly shared, yet they are available for research purposes from the corresponding author on reasonable request.

Human research participants

Policy information about studies involving human research participants and Sex and Gender in Research.

Reporting on sex and gender	The study did not involve human research participants.
Population characteristics	–
Recruitment	–
Ethics oversight	–

Note that full information on the approval of the study protocol must also be provided in the manuscript.

Field-specific reporting

Please select the one below that is the best fit for your research. If you are not sure, read the appropriate sections before making your selection.

☒ Life sciences ☐ Behavioural & social sciences ☐ Ecological, evolutionary & environmental sciences

For a reference copy of the document with all sections, see nature.com/documents/nr-reporting-summary-flat.pdf

Life sciences study design

All studies must disclose on these points even when the disclosure is negative.

Sample size	For the mapping of pancreatic innervation, at least 4 or 5 animals were used, on the basis of previously published studies (Fasanella et al. 2008, Quinson et al. 2001, Makhmutova et al. 2019). For AAV serotypes and delivery-route analysis, 5–7 animals were used, on the basis of previously published studies (Mason et al. 2010). For the in vitro Studies, 3 independent replicates were done per condition, as per previously reported studies on cell transfection (such as Takasugi et al. 2013). For in vivo metabolic studies, 7–16 mice were used, to detect statistical differences between groups (statistical power 0.8; effect size = 1.2 standard deviations; statistical significance, 0.05; two tailed) and based on previously published results (Moak et al. 2014, de Leon et al. 2018, Raun et al. 2020). For parasympathetic nerve ablation, 4 or 5 mice were used for the detection of statistical differences on the innervation density. Animal numbers were based on previously reported studies (Machado et al, 2020).
Data exclusions	Animals receiving misplaced injections were not included in the analysis.
Replication	All in vitro experiments were performed at least three times, for independent confirmation of the results. Viral tracing and metabolic animal studies were done at least using two cohorts. Information about replicates is included in the relevant figure legends. All attempts at replication were successful.
Randomization	All samples and all animals from the same litter were randomly allocated into experimental groups.
Blinding	Blinded data collection and analyses were conducted for the liver-de-targeting studies, for the in vivo metabolic analysis (the animals' IDs were decoded during the assays), for the Imaging analysis to compare viral titers, and for pancreatic innervation after targeted ablation. In vitro data acquisition could not be blinded because of the need to label the samples. Nevertheless, acquisition and analysis were performed using the same parameters for all the samples.

Reporting for specific materials, systems and methods

We require information from authors about some types of materials, experimental systems and methods used in many studies. Here, indicate whether each material, system or method listed is relevant to your study. If you are not sure if a list item applies to your research, read the appropriate section before selecting a response.

Materials & experimental systems

n/a	Involved in the study
☐	☒ Antibodies
☐	☒ Eukaryotic cell lines
☒	☐ Palaeontology and archaeology
☐	☒ Animals and other organisms
☒	☐ Clinical data
☒	☐ Dual use research of concern

Methods

n/a	Involved in the study
☒	☐ ChIP-seq
☒	☐ Flow cytometry
☒	☐ MRI-based neuroimaging

Antibodies

Antibodies used

For immunofluorescence staining the following primary antibodies were used: mCherry (Abcam, Cambridge, GBR; ab205402, Lot#GR3176028-11 dilution 1:1000), synapsin1 (D12G5) (Cell Signaling, Danvers, MA; 5297S, lot#07/2019, dilution 1:1000), GFP (AVES, Tigard, OR; GFP-1020 , Lot# 697986, at 1:1000 dilution), tyrosine hydroxylase (TH) (Millipore, Burlington, MA; AB152 , Lot#3328928, at 1:500 dilution), CTβ (Abcam, ab34992, Lot# GR3210643-1, at 1:500 dilution), Insulin (R&D, MAB1417, Lot# IDM0218121, at 1:1000 dilution)Vesicular Acetylcholine Transporter, Synaptic Systems, 139103 , Lot# 4-55, at 1:500 dilution). Somatostasin (SST, R210-01 ImmunoStar), Glucagon (SIGMA, G2624, Lot#0000080612), Gastrin Release Peptide, GRP (ImmunoStar, #20073, Lot#1420001), and Vasoactive Intestinal Peptide, VIP (ImmunoStar, #20077, Lot#2003001) at 1:500 dilution; cFOS (Abcam, # ab190289) at 1: 50. The secondary antibodies were: Alexa Fluor 647 anti-rabbit (Jackson ImmunoResearch, West Grove, PA; 711-605-152, Lot#139046), Alexa Fluor 546 anti-rabbit (Thermo Fisher Scientific; A10040, Lot#1946340), Alexa Fluor 647 anti-chicken (Jackson ImmunoResearch; 703-605-155, Lot#138591), Alexa Fluor 594 anti-mouse (ThermoFisher Scientific; A21203, Lot#1820087) ,Alexa Fluor 488 anti-guinea pig (Thermofisher Scientific; A11073, lot#2087691)and/or Alexa Fluor 488 anti-Rat (Thermofisher Scientific; A-21208, Lot#2092264) . All secondaries were diluted at 1:1000, with the exception of cFOS staining (Alexa Fluor 647 anti-rabbit at 1:50 dilution).

Validation

The information on antibody validation was taken from manufacturer's website(s), or through direct communication with the companies, as follows:

mCherry: Recombinant full length protein (His-tag) corresponding to mCherry. The immunogen sequence is from a following reference. Shaner NC et al. Nature Biotechnology 22:1567-1572 (2004).

Synapsin-1: (D12G5) XP® Rabbit mAb detects endogenous levels of total synapsin protein. The antigen is 100% conserved between human synapsin-1a and synapsin-1b. Monoclonal antibody is produced by immunizing animals with a synthetic peptide corresponding to residues surrounding Gln483 of human synapsin-1 protein. Relevant Citations: Wang Q et al 2022, Chen J et al 2021. According to Manufacturer's communication: 'Validation testing can include any of the following or combinations of the following: 1) Analysis of a large panel of cell lines with known target expression levels (high vs low expressors), 2) Treatment of cells with appropriate kinase-specific activators and/or inhibitors, 3) Phosphatase treatment 4) Correct subcellular localization or treatment-induced translocation 5) Comparison of results with antibody and isotype control to ensure acceptable signal-to-background ratio 6) Target-specific signal verified in transfected cells, knockout cells, or siRNA-treated cells 7) Blocking with antigen peptide to confirm elimination of specific signal.

GFP: According to manufacturer's website, Chickens were immunized with purified recombinant green fluorescent protein (GFP) emulsified in Freund's adjuvant. After multiple injections, eggs were collected from the hens, and IgY fractions were prepared from the yolks and then affinity-purified antibodies were prepared using GFP conjugated to an agarose matrix. The final product is a filter-sterilized mixture of both affinity-purified antibodies (30 µg/mL) and purified IgY (10 mg/mL). To validate the product, manufacturer states: Antibodies were analyzed by western blot analysis (1:5000 dilution) and immunohistochemistry (1:500 dilution) using transgenic mice expressing the GFP gene product. Western blots were performed using BlokHen® (Aves Labs) as the blocking reagent, and HRP-labeled goat anti-chicken antibodies (Aves Labs, Cat. #H-1004) as the detection reagent. Immunohistochemistry used tetramethyl rhodamine-labeled anti-chicken IgY. Anti-Tyrosine Hydroxylase Antibody detects level of TH and has been published and validated for use in ELISA, IF, IH, IH(P), IP and WB. Manufacturer's website states that this antobody is routinely evaluated by Western Blot on PC12 lysates.

CTb: Rabbit polyclonal to beta subunit Cholera Toxin. Relevant citations: Song SY et al 2020, Sieveritz Bet al 2020, Lan H et al 2020. Insulin: Immunogen to E. coli-derived recombinant human Insulin. Detects bovine, human, and mouse insulin. Relevant citations: Rui J et al 2021, Elizondo DM et al 2020.

VACHT: According to manufacturer's website, This antibody detects the glycosylated and unglycosylated protein and is an excellent marker for cholinergic axons. Reacts with: human (Q16572), rat (Q62666), mouse (O35304), pig. Other species not tested yet. Specific for VAChT. (K.O. verified). Communication from the manufacturer: 'The antibody has been tested transfected and untransfected cells and only stains VachT transfected cells. It shows a band of expected molecular weight that is enriched in synaptic vesicle fraction. It shows the expected staining patter on cultured neurons and tissue sections.It has been KO validated for WB in this publication: https://pubmed.ncbi.nlm.nih.gov/24027290/'.Relevant citations: Martin-Silva C et al 2011, Teixiera VP et al 2020.

SOMATOSTATIN:According to manufacturer's website, The specificity of the antiserum was examined by soluble preadsorption with the peptides at a final concentration of 106 M. Somatostatin immunolabeling was completely abolished by preadsorption with somatostatin, somatostatin 25, and somatostatin 28. Preadsorption with the following peptides resulted in no reduction of immunostaining: substance P, amylin, glucagon, insulin, neuropeptide Y, and VIP. Relevant citations are: Chiazza F et al, 2021, An J.J et al 2020, Valbuena S et al 2019.

VIP: According to manufacturer's website, The specificity of the antiserum was examined by soluble pre-adsorption with the peptides in question at a final concentration of 10-5 M. VIP immunolabeling was completely abolished by pre-adsorption with VIP. Pre-adsorption with the following peptides resulted in no reduction of immunostaining: Secretin, gastric inhibitory polypeptide, somatostatin, glucagon, insulin, ACTH, gastrin 34, FMRF-amide, rat GHRF, human GHRF, peptide histidine isoleucine 27, rat pancreatic polypeptide, motilin, peptide YY, substance P, neuropeptide Y, and CGRP. Relevant citations are: Mukherjee A et al 2021, Ferraro S et al 2021,

GRP: The ImmunoStar Gastrin Releasing Peptide antiserum was quality control tested using standard immunohistochemical methods. The antiserum demonstrates strongly positive labeling of rat dorsal horn of spinal cord using indirect immunofluorescent and biotin/avidin-HRP techniques. Recommended primary dilution is 1/1,000-1/2,000 in PBS/0.3% Triton X-100 – Bn/Av-HRP Technique. Staining is completely eliminated by pretreatment of 1 mL of diluted antibody with 50 µg of bombesin. Relevant citations: Mou H et al 2021, Hamnett R et al 2021.

Eukaryotic cell lines

Policy information about cell lines and Sex and Gender in Research

Cell line source(s)	Human embryonic kidney cells (HEK 293T) (ATCC CRL-3216, mycoplasma testing and STR profiling performed by ATCC). Neuro2A (ATCC CCL-131, mycoplasma testing and STR profiling performed by ATCC). AML12 cells (ATCC CRL-2254, mycoplasma testing and STR profiling performed by ATCC).
Authentication	STR analysis was performed by ATCC on all the human cell lines that we used.
Mycoplasma contamination	We did not test the cell lines for mycoplasma contamination.
Commonly misidentified lines (See ICLAC register)	No commonly misidentified cell lines were used.

Animals and other research organisms

Policy information about studies involving animals; ARRIVE guidelines recommended for reporting animal research, and Sex and Gender in Research

Laboratory animals	Male and female WT C57BL/6J, heterozygous ChAT-IRES-Cre, and Snap25-2A-GCaMP6s-D on a C57BL/6 background (Jackson Laboratories; #000664, #028861 and #025111, respectively) aged 8–12 weeks were used, and maintained with access to food ad-libitum. All mice were housed in a temperature-controlled environment (20–22 Celsius, 50–60% humidity) with twelve hours of light per day at the Center for Comparative Medicine and Surgery (CCMS) at the Icahn School of Medicine at Mount Sinai (New York, NY, USA).
Wild animals	The study did not involve wild animals.
Reporting on sex	Sex was considered in the study design for the initial in vivo metabolic studies. Male and female mice were age-matched and were subjected to the same experimental protocol. Data from chemogenetic stimulation of pancreatic parasympathetic nerves were disaggregated for sex. Only males presented significant differences. Therefore, the remaining of metabolic studies were performed in males.
Field-collected samples	The study did not involve samples collected from the field.
Ethics oversight	All animal studies were performed with the approval of, and in accordance with, guidelines established by the Icahn School of Medicine at Mount Sinai, and principles of laboratory animal care were followed. The IACUC protocol was reviewed and approved by the Institutional Animal Care and Use Committee of the Icahn School of Medicine at Mount Sinai.

Note that full information on the approval of the study protocol must also be provided in the manuscript.